Neutral hydrogen and magnetic fields in M83 observed with the SKA Pathfinder KAT-7

Heald, G.; de Blok, W. J. G.; Lucero, D.; Carignan, C.; Jarrett, T.; Elson, E.; Oozeer, N.; Randriamampandry, T. H.; van Zee, L.

Published in:
Monthly Notices of the Royal Astronomical Society

DOI:
10.1093/mnras/stw1698

Publication date:
2016

Monthly Notices
of the
ROYAL ASTRONOMICAL SOCIETY

MNRAS **462,** 1238–1255 (2016)
Advance Access publication 2016 July 14

doi:10.1093/mnras/stw1698

Neutral hydrogen and magnetic fields in M83 observed with the SKA Pathfinder KAT-7

G. Heald,[1,2,3]★ W. J. G. de Blok,[2,4,3] D. Lucero,[4] C. Carignan,[4,5] T. Jarrett,[4] E. Elson,[4] N. Oozeer,[6,7,8] T. H. Randriamampandry[4] and L. van Zee[9]

[1]*CSIRO Astronomy and Space Science, 26 Dick Perry Avenue, Kensington, WA 6151, Australia*
[2]*ASTRON, the Netherlands Institute for Radio Astronomy, Postbus 2, NL-7990 AA Dwingeloo, the Netherlands*
[3]*Kapteyn Astronomical Institute, University of Groningen, PO Box 800, NL-9700 AV Groningen, the Netherlands*
[4]*Department of Astronomy, University of Cape Town, Private Bag X3, Rondebosch 7701, South Africa*
[5]*Observatoire d'Astrophysique de l'Université de Ouagadougou, BP 7021, Ouagadougou 03, Burkina Faso*
[6]*SKA South Africa, The Park, Park Road, Pinelands, Cape Town 7405, South Africa*
[7]*African Institute for Mathematical Sciences, 6-8 Melrose Road, Muizenberg 7945, South Africa*
[8]*Centre for Space Research, North-West University, Potchefstroom 2520, South Africa*
[9]*Astronomy Department, Indiana University, IN 47405, USA*

Accepted 2016 July 12. Received 2016 July 4; in original form 2016 May 16

ABSTRACT

We present new KAT-7 observations of the neutral hydrogen (H I) spectral line, and polarized radio continuum emission, in the grand-design spiral M83. These observations provide a sensitive probe of the outer-disc structure and kinematics, revealing a vast and massive neutral gas distribution that appears to be tightly coupled to the interaction of the galaxy with the environment. We present a new rotation curve extending out to a radius of 50 kpc. Based on our new H I data set and comparison with multiwavelength data from the literature, we consider the impact of mergers on the outer disc and discuss the evolution of M83. We also study the periphery of the H I distribution and reveal a sharp edge to the gaseous disc that is consistent with photoionization or ram pressure from the intergalactic medium. The radio continuum emission is not nearly as extended as the H I and is restricted to the main optical disc. Despite the relatively low angular resolution, we are able to draw broad conclusions about the large-scale magnetic field topology. We show that the magnetic field of M83 is similar in form to other nearby star-forming galaxies, and suggest that the disc–halo interface may host a large-scale regular magnetic field.

Key words: galaxies: evolution – galaxies: individual: M83 – galaxies: ISM – galaxies: kinematics and dynamics – galaxies: magnetic fields.

1 INTRODUCTION

The evolution of galaxies is strongly influenced by their connection to the surrounding environment. Whether the dominant effect is in the form of gas accretion (Sancisi et al. 2008), dynamical interactions (e.g. Boselli & Gavazzi 2006), or mergers (e.g. Blanton & Moustakas 2009), it is in the outskirts of galaxies where these evolutionary effects are clearly visible and traceable. Investigation of these effects is key to understanding the mechanisms by which galaxies continue to grow, or cease growing (see for example Putman, Peek & Joung 2012).

In the outer parts of galaxies, neutral hydrogen (H I) has long been recognized as an excellent tracer of the effects listed above. As a necessary ingredient for future star formation (SF), such material also represents an indication for the potential for continued evolution. By contrast, an ingredient of galactic outskirts whose role is not currently understood is the magnetic field content. Magnetic fields associated with the star-forming discs of galaxies are fairly well understood (e.g. Beck 2016). However, the properties of magnetic fields in the outer parts of galaxies can so far only be inferred from large-scale synchrotron polarization patterns (Braun, Heald & Beck 2010), or from polarization properties of distant background radio galaxies (Bernet, Miniati & Lilly 2013). Whether the magnetic content of galaxy outskirts is important dynamically (Benjamin 2000; Elstner, Beck & Gressel 2014; Henriksen & Irwin 2016, and references therein) or energetically (cf. Beck 2007) remains unclear.

Probing the outer parts of galaxies can be a difficult observational endeavour because the mass distribution is often extended

★ E-mail: george.heald@csiro.au.

over a large area. Careful observations with very high sensitivity to low surface brightness features are typically required. While great strides in this direction have been made during recent years, future radio telescopes will provide new capabilities to facilitate this line of research, both for H I and magnetism. Amongst the telescopes that are anticipated in the next few years, two that will provide a large instantaneous field of view (FoV) are the Australian Square Kilometre Array Pathfinder (ASKAP, Johnston et al. 2008) and the Aperture Tile in Focus (APERTIF, Verheijen et al. 2008) upgrade to the Westerbork Synthesis Radio Telescope (WSRT). A different approach to bolster the speed needed to complete a large survey has been adopted by the Karoo Array Telescope (MeerKAT; Jonas 2009). This latter telescope, despite its comparatively small instantaneous FoV, will nevertheless be particularly well suited for high sensitivity (including low column density) observations over large areas on the sky. For this reason, several MeerKAT surveys are planned that typically aim to probe samples of very faint or distant galaxies (see Booth & Jonas 2012). The prospect of combining MeerKAT with the Five hundred metre Aperture Spherical radio Telescope (FAST, Nan et al. 2011) holds the promise of extremely sensitive observations that may probe the galaxy–intergalactic medium (IGM) interface (Carignan 2016).

One of the several forthcoming MeerKAT surveys that are currently planned is named 'MeerKAT H I Observations of Nearby Galactic Objects: Observing Southern Emitters' (MHONGOOSE).[1] The motivation and design of MHONGOOSE is similar in many respects to the recent WSRT Hydrogen Accretion in LOcal GAlaxieS (Heald et al. 2011) survey. Specifically, MHONGOOSE will perform deep H I observations of 30 nearby galaxies, achieving column density sensitivities of several $\times\ 10^{18}$ atoms cm^{-2} at kpc-scale physical resolution. MHONGHOOSE will build on the capability of most existing H I surveys by also providing excellent polarization data along with the spectral line cubes, thus enabling investigation of the magnetic fields along with the gas morphology and kinematics. As the community prepares for data and science results from MHONGOOSE, initial exploratory observations are being performed with the KAT-7 radio telescope (see, e.g. Hess et al. 2015; Lucero et al. 2015; Carignan et al. 2016), which is the precursor radio telescope located on the MeerKAT site in South Africa (Carignan et al. 2013).

M83 (NGC 5236) is a grand-design spiral galaxy at the centre of a loose group (Karachentsev et al. 2007). M83 is a prominent example of an interesting class of galaxies showing extended UV (XUV) emission (Thilker et al. 2005, 2007), indicative of active SF taking place out to several optical radii (nearly $4 \times r_{25}$). What fuels this outer-disc SF? Recent H I observations of M83 have been obtained with the Australia Telescope Compact Array (ATCA, Park et al. 2001; Jarrett et al. 2013) and with the Very Large Array (VLA; de Blok et al. 2008; Walter et al. 2008; Barnes et al. 2014). These reveal a very extended H I distribution that also reaches far beyond the main optical disc, and with a very close morphological correlation between sites of recent SF and high-column density regions in the H I reservoir (Bigiel et al. 2010). With the available data, Bigiel et al. (2010) were able to constrain the outer-disc gas depletion time from *in situ* SF to of the order of 100 Gyr. In this paper, we present new H I observations that reveal even more neutral gas mass in the outer disc than has been seen previously, strengthening the conclusion that a vast, nearly untapped gas mass resides outside of the main disc in this galaxy, and may provide a source of fuel to maintain SF occurring within the central star-forming disc. We summarize some basic properties of M83 in Table 1.

This paper is organized as follows. We describe the KAT-7 data collection and reduction procedures in Section 2. The data are described in Section 3, where we present new details about the H I distribution and kinematics, along with their connection to stellar features in the outer disc and to the environment more generally. We also present new conclusions regarding the large-scale magnetic field structure in M83 (Section 4). We conclude the paper in Section 5.

2 DATA AND REDUCTION

Our KAT-7 observations were designed to make use of the telescope's flexible correlator capabilities (see Carignan et al. 2013) in order to study both the neutral gas content and the magnetic fields in M83. In these commissioning observations, we observed the target galaxy in several sessions, using two different modes (full-polarization broad-band, and spectral line). MeerKAT observations will allow these to be recorded simultaneously. In this section, we describe how the KAT-7 data were obtained and how the data reduction was performed. A summary of the observations is given in Table 2.

2.1 Wideband mode

Our first KAT-7 observations were performed in a wideband, full-polarization correlator mode. These continuum observations utilized the c16n400M4K correlator mode. This mode consists of a 400 MHz band with 1024 390.625 kHz channels (of which approximately 650 channels, ∼256 MHz, are useable). The correlator was tuned to a centre frequency of 1328 MHz. The data provide correlations in full polarization. The data are interleaved with the gain calibrator (PKS 1313−333; see Table 3). Additional calibrators for primary flux and bandpass calibration (PKS 1934−638) and polarization (3C138 and 3C286) were also observed for short periods during the observing run.

Known unwanted channels and radio frequency interference (RFI) were flagged automatically using a specialized online routine developed by the KAT-7 team. An additional flagging step to eliminate visibilities corresponding to elevation lower than 20° was also performed. Clipping using the CASA (McMullin et al. 2007) task `tflagdata` was done manually by looking at the cross-polarization correlations. After successful flagging, the data were calibrated using PKS J1934−638 for primary calibration, and PKS 1313−333 as the phase calibrator. The cross-hand delays and phase solutions were determined using 3C286 as the polarization calibrator by assuming a zero polarization model. Following calibration, we recovered for 3C286 a polarization fraction of 8.7 ± 0.1 per cent and electric vector position angle of $29.9 \pm 2.^{\circ}5$. These extracted values agree reasonably well with the expected values at 1372 MHz (≈9.3 per cent and 33°, respectively; see Perley & Butler 2013).

Images were created for each Stokes parameter in CASA and deconvolved using a `CLEAN` mask defined by sources catalogued brighter than 10 mJy by the NRAO VLA Sky Survey (NVSS, Condon et al. 1998). Spectral line cubes were produced for Stokes parameters Q and U, with frequency resolution 1.5625 MHz and synthesized beam size 244 arcsec × 230 arcsec. Further analysis steps are described in Section 4.

[1] PI de Blok; see http://mhongoose.astron.nl/.

Table 1. Properties of M83.

Property	Value	Reference
Hubble type	SAB(s)c	de Vaucouleurs et al. (1991)
Distance	4.79 Mpc (43.1 arcsec = 1 kpc)	Karachentsev et al. (2007)
D_{25}	11.7 arcmin	Tully (1988)
M_B	−20.94	Makarov et al. (2014)
SFR (12 μm)	$4.95 \pm 0.09\,M_\odot\,yr^{-1}$	Jarrett et al. (2013); Cluver et al. (2014)
SFR (22 μm)	$3.86 \pm 0.07\,M_\odot\,yr^{-1}$	Jarrett et al. (2013); Cluver et al. (2014)
Total H I mass	$9.0 \times 10^9\,M_\odot$	This work
Stellar mass	$2.88 \times 10^{10}\,M_\odot$	Jarrett et al. (2013); Cluver et al. (2014)
Virial mass	$2 \times 10^{12}\,M_\odot$	Tully (2015)
Systemic velocity	$510\,km\,s^{-1}$	This work
Maximum rotational velocity	$170\,km\,s^{-1}$	This work

Table 2. KAT-7 observations of M83.

Date/time	Number of antennas	On-source time (h)	Mode	Mosaic?
2013 July 29	7	7.6	Wideband	N
2014 March 2–3	6	10.7	Line	Y
2014 April 15–16	7	7.4	Line	Y
2014 April 16–17	7	7.0	Line	Y
2014 April 18	7	5.5	Line	Y
2014 April 20	7	5.5	Line	Y
2014 April 22	7	3.6	Line	Y
2014 April 25	7	3.7	Line	Y

2.2 Line mode

Subsequent observing sessions focused on the neutral hydrogen line emission. Our KAT-7 H I observations utilized the c1625M4k correlator mode. This mode gives an instantaneous bandwidth of 6.25 MHz and 4096 channels each 1.525 879 kHz in width. The correlator was tuned to a centre frequency of 1422.8 MHz. We used three mosaic pointings to cover the full angular extent of the H I disc. These pointings are summarized in Table 4. The observations were set up to observe each pointing in turn for approximately 8 min each, followed by a gain calibrator (again PKS 1313−333; see Table 3). During each session, the gain calibrator was observed 12–14 times. The average flux density of the gain calibrator, as measured after bootstrapping the flux calibration from PKS 1934−638, is in every session within 8 per cent of the nominal value given in Table 3. The KAT-7 line data sets provide all four correlations but here we consider the parallel hands (HH and VV) only.

Calibration was performed independently for all observing epochs. We used CASA version 4.2.2 for the initial steps and then transitioned to MIRIAD for self-calibration and final imaging (both for the continuum and the H I cubes).

Data flagging (e.g. RFI spikes, antenna shadowing) was performed by hand using the CASA task `flagdata`. The primary (flux and bandpass) calibration was achieved using PKS 1934−638, and subsequent gain calibration (sensitivity and phase variation) was determined using PKS 1313−333. Properties of these calibrators are given in Table 3. At this point, offline Doppler correction was performed for the line data since it is not implemented in the correlator. Next, visibilities with (u, v) coordinates satisfying the condition $|u| < 5.25m \approx 25\lambda$ were removed from the data set, even for large values of v. This is needed due to an issue, possibly related to internally generated RFI, that causes such visibilities have an overly high amplitude, resulting in horizontal stripes in the image plane. In our data, this preemptive step typically removes about 4–8 per cent of the visibilities, and should not affect our ability to recover extended structures (spacings shorter than 25λ pick up structures larger than ≈2.°3, which we do not expect in M83). Moreover, the step that limits the largest accessible angular scale in practice is the flagging for antenna shadowing, which impacts angular scales larger than ≈0.°95. Next, the data are exported to MIRIAD (Sault, Teuben & Wright 1995).

Table 4. KAT-7 line-mode mosaic pointings for M83.

Pointing code	RA (J2000)	Dec. (J2000)
M83-N	$13^h37^m00^s.9$	$-29^d26^m56^s.0$
M83-C	$13^h37^m00^s.9$	$-29^d51^m55^s.5$
M83-S	$13^h37^m00^s.9$	$-30^d16^m56^s.0$

Continuum subtraction was performed in the *uv* domain using task `uvlin` by fitting the spectrum of each visibility record with a second-order polynomial and subtracting the fit from the data. The corresponding 'channel-0' (frequency-averaged) visibilities computed from the fitted polynomials were imaged to form a broad-band continuum image. That image was deconvolved with the `CLEAN` algorithm, and a model based on the `CLEAN` components was used to update the phase calibration with a time-scale of 2 min. Subsequently, a single gain amplitude solution was determined per antenna polarization, per 8 min scan, in each mosaic field. These gain amplitudes were normalized to preserve the flux scale. The resulting high-quality set of gain solutions was transferred to the continuum-subtracted line data. The final continuum image was

Table 3. Calibrators for M83 data sets.

Calibrator	RA (J2000)	Dec. (J2000)	Flux density (Jy)	Reference	Purpose
PKS 1313−333	$13^h16^m08^s.0$	$-33^d38^m59^s$	1.13	Tingay et al. (2003)	Gain
PKS 1934−638	$19^h39^m25^s.0$	$-63^d42^m46^s$	14.98	Tingay et al. (2003)	Bandpass
3C138	$05^h21^m09^s.9$	$+16^d38^m22^s$	8.47	VLA calibrator manual	Polarization
3C286	$13^h31^m08^s.3$	$+30^d30^m33^s$	15.00	VLA calibrator manual	Polarization

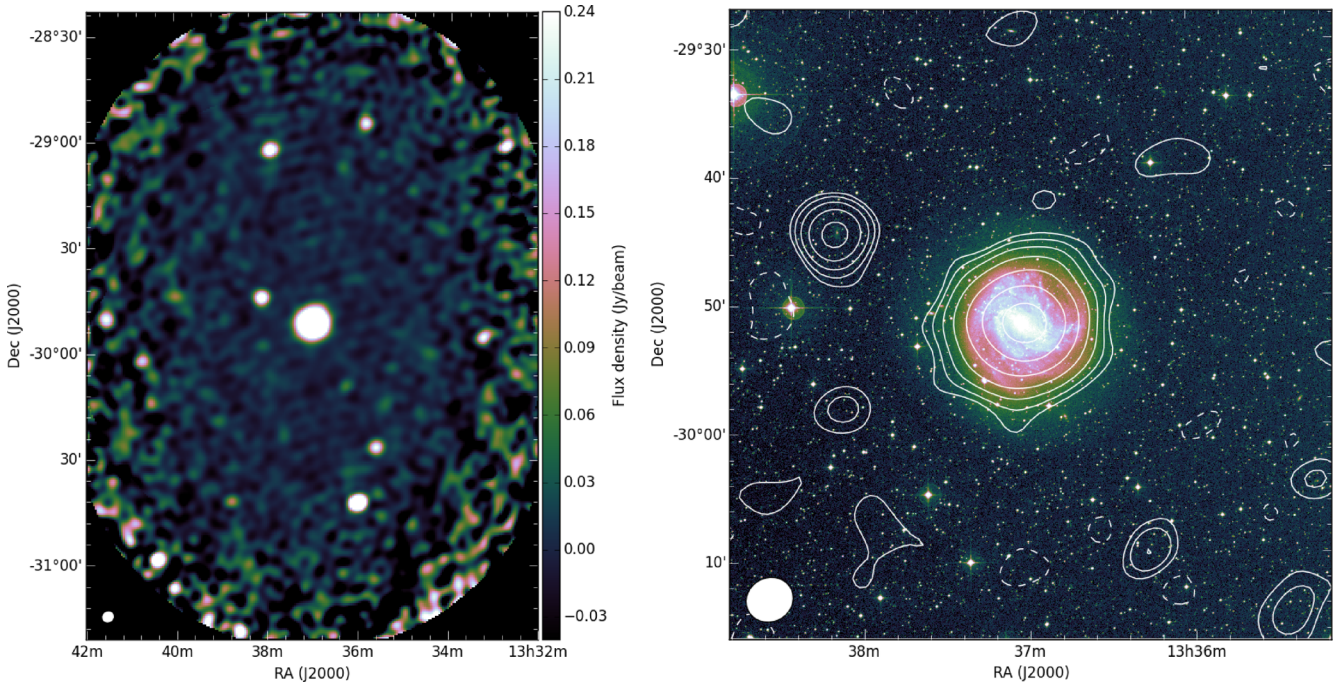

Figure 1. Continuum images of the M83 field, based on the line data. Left: continuum mosaic displayed using the cubehelix colourmap. The 225 arcsec × 205 arcsec synthesized beam is shown in the bottom left. Right: optical image (DSS-II red) on a square root stretch, overlaid with contours from the same continuum map. Contours begin at 16 mJy beam^{-1} ($\approx 2\sigma$) and increase by powers of two. The -2σ level is also displayed with dashed contours. The bright continuum source to the northeast of M83 is a background galaxy cluster, MCXC J1338.0−2944, located at $z = 0.189$ (Piffaretti et al. 2011).

produced using multifrequency synthesis; that image is shown in Fig. 1.

Finally, the line data were imaged, Hanning smoothed, and deconvolved. We used the task `mossdi` for deconvolving the line cubes. This task performs Steer CLEAN (Steer, Dewdney & Ito 1984). The deconvolution used a threshold of approximately 0.5σ and a carefully defined mask (consisting of regions obtained by masking a smoothed version of an earlier cube, rather than boxes). The CLEAN mask was derived over several iterations of the H I cube, each with a progressively improved deconvolution and accompanying mask quality.

In order to successfully perform the mosaicking for the line data, the primary beam needs to be specified. We estimated the beam to have a Gaussian profile with a half power beam width (HPBW) given by

$$\mathrm{HPBW} = \alpha \frac{\lambda}{D}, \quad (1)$$

where λ is the observing wavelength, D is the dish diameter, and α is a factor related to the tapering of the dish. The latter is found empirically to have a value of $\alpha = 1.27$ for KAT-7, based on holographic measurements (Foley et al. 2016). Along with $\lambda = 0.21$ m and $D = 12$ m, we obtained HPBW = 4580 arcsec = 1.°27. The mosaicking was performed in practice using MIRIAD tasks `invert` with option `mosaic` for initial imaging and the deconvolution task `mossdi` as described above. To perform the final primary beam correction, we used the task `mossen` to determine the effective combined sensitivity map and `maths` to apply it to the cubes.

The *uv* coverage of the observations is shown in Fig. 2. The effect of the $u < 25\lambda$ flagging step is plainly visible. Note that while the *uv* plane is well filled by our tracks, due to the layout

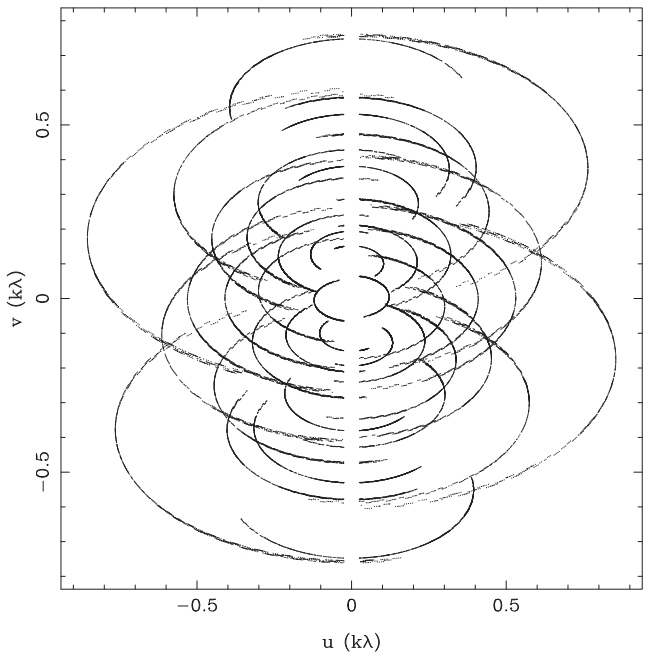

Figure 2. UV coverage of the M83 observation. The three mosaic pointings are clearly distinguishable on the longer baselines. Only every eleventh point is plotted.

of the array there is no strong overdensity of points at the shorter spacings. We found that differences in image-plane resolution and image noise were minimal for a wide range of visibility weighting (robust; see Briggs 1995) parameters. Thus we use a single cube

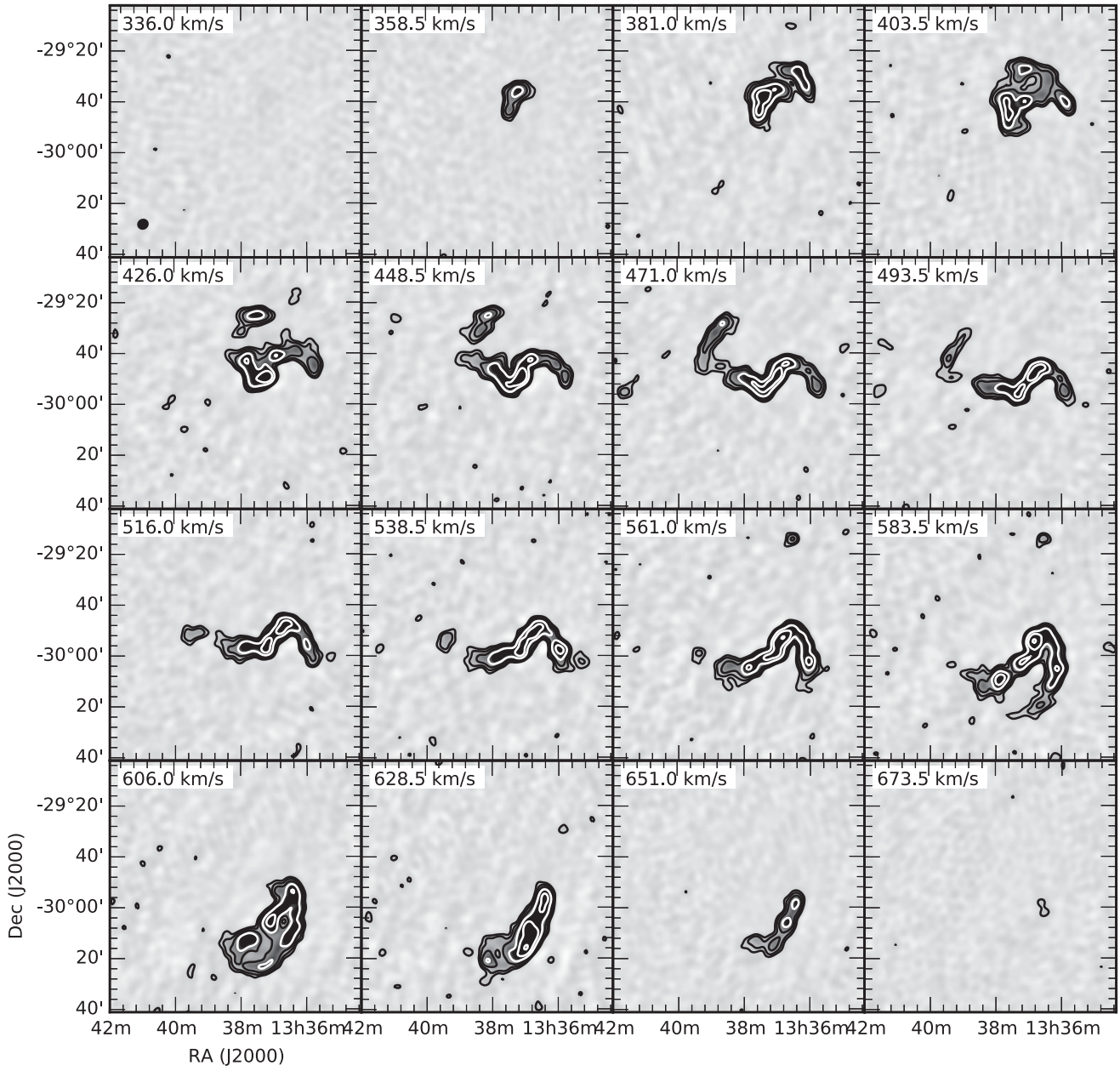

Figure 3. Channel maps. Levels start at 25 mJy beam^{-1} and increase by powers of two. The velocity of the shown channels is displayed in the upper left of each panel. Only every fifteenth 1.5 km s^{-1} channel is shown. The synthesized beam size is shown with a black ellipse in the bottom-left corner of the top-left frame.

for the analysis in this paper, produced using a robust parameter of +0.5 and a channel width of 1.5 km s^{-1}. The synthesized beam size is 225 arcsec × 205 arcsec. The noise level per channels is typically 5.0 mJy beam^{-1}, and this corresponds to a 3σ column density sensitivity of $N_{\rm H\,II} = 5.6 \times 10^{18}$ cm^{-2} for a 16 km s^{-1} line width. Channel maps from the H I cube are shown in Fig. 3. These properties are summarized in Table 5.

Table 5. M83 H I data cube properties.

Robust parameter	+0.5
Channel width (km s^{-1})	1.5
Beam size (arcsec)	225 × 205
Beam angle (°)	−61
Noise level (mJy beam^{-1})[a]	5.0
$N_{\rm H\,I}$ sensitivity[b] (atoms cm^{-2})	5.6×10^{18}

[a]Per 1.5 km s^{-1} channel.
[b]Corresponding to 3σ over a summed line width of 16 km s^{-1}.

2.3 Multiwavelength supplementary data

2.3.1 GALEX

We make use of deep GALEX images extracted from the archive. The deep FUV and NUV images were obtained through programme

GI3_050007 and included 14 256.4 s in NUV and 14 250.4 s in FUV observed between 2007 March 15 and 2008 March 16. To enhance extended emission associated with SF in the outer parts of M83, we smooth both FUV and NUV images to 10 arcsec resolution.

2.3.2 *WISE*

Wide-Field Infrared Survey Explorer (*WISE*) imaging has proven to be a very effective tool to study the SF history of nearby galaxies (Jarrett et al. 2013), owing in part to the (arbitrarily) large FoV and photometric bands that cover both the stellar (3.4 and 4.6 μm, or the *W*1 and *W*2 bands) and gas/dust components (12 and 22 μm, or *W*3 and *W*4 bands). To study M83's disc and greater environment, we constructed dedicated *WISE* mosaics using a 'drizzle' sampling technique (Jarrett et al. 2012) that conserves the native angular resolution while providing full coverage of the field. The resulting *WISE* mosaics cover the galaxy and its dynamic environment, over 4 square degrees.

Global measurements of the star-forming disc were carried out using the characterization pipeline of the *WISE* Enhanced Resolution Atlas (Jarrett et al. 2013). Foreground stars were identified and point spread function-subtracted, the disc shape of M83 was determined and surface brightness was extracted. The 3.4 μm (*W*1) 1σ (23.07 mag sq. arcsec^{-1} in Vega, or 25.82 mag sq. arcsec^{-1} in AB) isophotal diameter is 18.7 arcmin with an axis ratio of 0.938. The corresponding integrated flux densities are 6.24, 3.79, 21.65 and 43.66 Jy, for *W*1, *W*2, *W*3 and *W*4, respectively.

Demonstrated in Jarrett et al. (2013) and updated in Cluver et al. (2014), the stellar mass-to-light (M/L) ratio has a simple dependence on the [*W*1–*W*2] colour. Assuming our adopted distance of 4.79 Mpc to M83, the corresponding *W*1 absolute magnitude and in-band luminosity L_{W1} are −24.16 and 9.120×10^{10} L$_\odot$, respectively. The *W*1–*W*2 colour is 0.12 ± 0.02 mag, and employing the nearby-galaxy M/L relation from Cluver et al. (2014), the inferred stellar mass is then $3.020 \pm 0.390 \times 10^{10}$ M$_\odot$, representing the evolved stellar population that corresponds to the past SF history of M83.

The obscured SF activity may be estimated by the *WISE* 12 and 22 μm luminosities, νL_ν, which are 4.07×10^9 and 4.17×10^9 L$_\odot$, respectively. Correspondingly, we apply the relations in Cluver et al. (2014) to infer the dust-obscured star formation rate (SFR): 5.2 and 4.1 M$_\odot$ yr^{-1}, respectively, based on the 11.3 μm polycyclic aromatic hydrocarbon emission and the 22 μm dust continuum. These new SFRs are comparable (within the uncertainties) to the total UV+IR value given by Jarrett et al. (2013), namely 3.2 M$_\odot$ yr^{-1}. In the Local Volume among disc galaxies, the M83 global SFR is significant, within a factor of ∼2 of the notable starbursts M82 and NGC 253 (Lucero et al. 2015).

Finally, normalizing the SFR with the stellar mass, the resulting specific SFR is 1.74×10^{-10} and 1.35×10^{-10} yr^{-1}, derived from *W*3 and *W*4, respectively. Indicative of the large SFR, this disc building rate is relatively high for local galaxies, comparable to other large star-forming spirals, including NGC 253 and NGC 6946 (Jarrett et al. 2013).

3 NEUTRAL GAS DISTRIBUTION

3.1 General properties

Based on our KAT-7 H I data cube, we construct a global velocity profile as shown in Fig. 4. The distribution is clearly asymmetric, as has been observed previously. We find that 45 per cent of the total H I mass is on the approaching side, and 55 per cent on the receding side. Fig. 5 compares the H I radial surface density profile obtained with KAT-7 with those derived from the VLA data of de Blok et al. (2008) and Barnes et al. (2014). The flux recovered by KAT-7 on large scales is clearly recognized.

The total mass of H I from our KAT-7 observations is $M_{\rm HI} = 9.0 \times 10^9$ M$_\odot$, assuming a distance of 4.79 Mpc (Karachentsev et al. 2007). From the literature, the single-dish H I mass is reported to be 8.8×10^9 M$_\odot$ (Huchtmeier & Bohnenstengel 1981), or 8.9×10^9 M$_\odot$ from HIPASS (Koribalski et al. 2004, see corresponding global profile in Fig. 4), both corrected for distance.

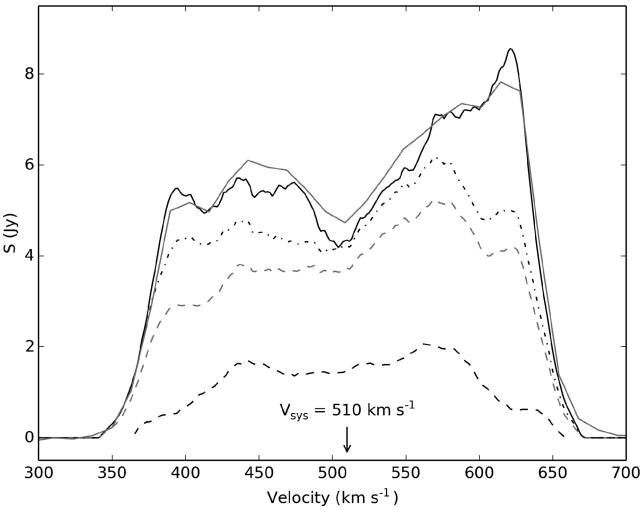

Figure 4. Global H I profile of M83 from our KAT-7 observations (solid black line). The profile from THINGS is also shown for comparison (dashed black line); here, only about 20 per cent of the KAT-7 flux density is recovered. The global profile derived by only including H I emission from the KAT-7 data within the 20 per cent response of the VLA primary beam is also shown for reference (dot–dashed line), as is the global profile derived by masking the KAT-7 cube using the THINGS moment-0 map (dashed grey line). Finally, the HIPASS global profile from Koribalski et al. (2004) is also displayed (solid grey line). The systemic velocity appropriate for the centre of the galaxy is indicated with an arrow.

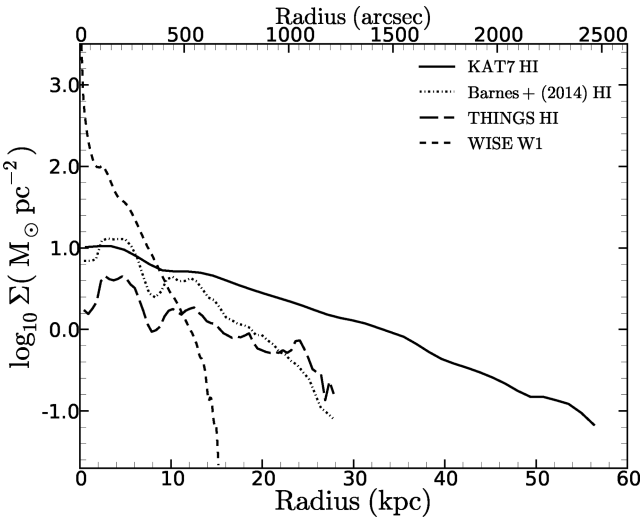

Figure 5. Comparison of the H I radial surface density profiles between the KAT-7 data and the VLA data from de Blok et al. (2008) and Barnes et al. (2014). Also shown is the *WISE W*1 radio profile.

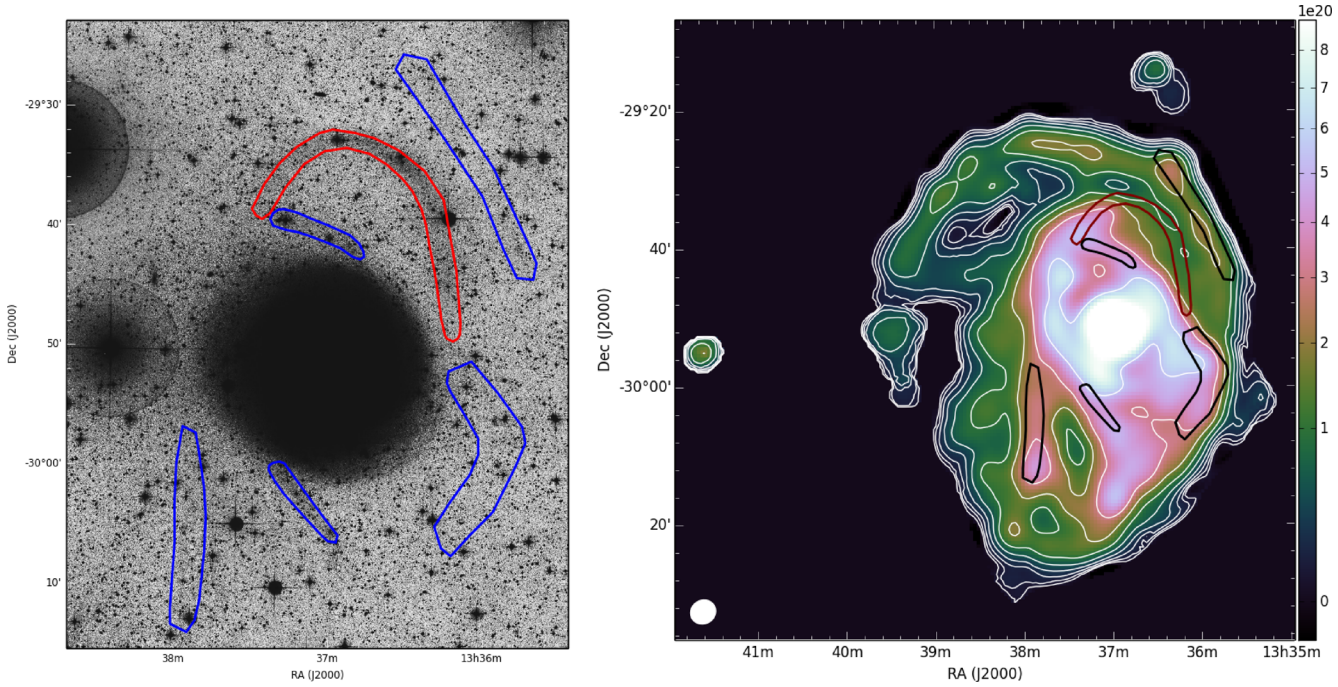

Figure 6. Left: deep image derived from plates taken with the UK Schmidt telescope, courtesy of David Malin (see Malin & Hadley 1997), with stellar stream highlighted in red and outer-disc star-forming arms highlighted in blue. Right: neutral hydrogen column density distribution. Contours start at 5.6×10^{18} cm^{-2} and increase by powers of 1.778. Highlighted regions are the same as in the left-hand panel. The beam size is displayed with a white ellipse in the bottom-left corner of the panel.

This implies that we recover all of the H I mass in the system with our KAT-7 observations. The H I column density map is displayed in Fig. 6. The column density contours are overlaid on the *WISE* multicolour image in Fig. 8. Plainly, the outer H I envelope is greatly extended beyond the bright optical disc. The size of the H I disc is larger than seen previously in interferometric observations, as demonstrated in Fig. 7 in which we compare with the high-resolution (but single-pointing) map from THINGS (Bigiel et al. 2010). The improved recovery of outer-disc H I comes from a combination of factors: larger FoV per pointing, the mosaic observations that we have employed, and excellent sensitivity to low surface brightness emission (see also Lucero et al. 2015). It also leads to the KAT-7 observations having recovered substantially more H I mass than the THINGS observations. In Fig. 4, we have illustrated the reason for this in two ways: (i) the global H I profile that would result by filtering the KAT-7 data cube with the VLA primary beam; (ii) the global H I profile that results by masking the KAT-7 data cube with the THINGS moment-0 map. Clearly, the FoV explains some of the H I mass missed by THINGS, but not all. With KAT-7, we recover the same radial distribution of H I as was implied by the single-dish Effelsberg map from Huchtmeier & Bohnenstengel (1981), which we checked by smoothing the KAT-7 column density map to 9 arcmin resolution and performing a direct comparison.

In Fig. 8, it is apparent that the M83 field contains some additional galaxies that are associated with M83 itself. The companion galaxy visible to the east is NGC 5264. The companion to the north is catalogued as E444-78 (UGCA 365). There is also an object present in the outer H I disc, catalogued by Karachentseva & Karachentsev (1998) as KK 208. We return to this interesting object in Section 3.4.

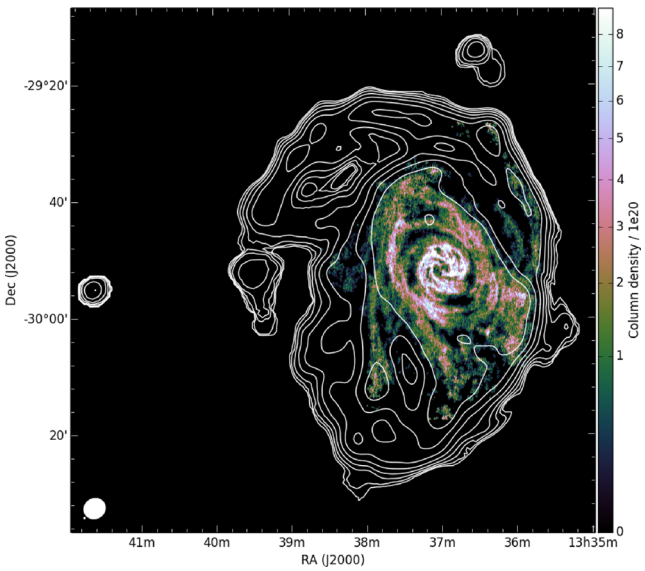

Figure 7. Naturally weighted H I column density map of M83 from THINGS (Walter et al. 2008) data, as used by Bigiel et al. (2010). The KAT-7 contours are overlaid, and demonstrate an excellent morphological agreement despite the vastly different angular resolution, as well as the presence of far more neutral gas in the outer parts in our new observations than has previously been studied. The contour levels are the same as in Fig. 6. The beam sizes are shown in the bottom-left corner for the KAT-7 data (large white ellipse) and the VLA data (small white ellipse).

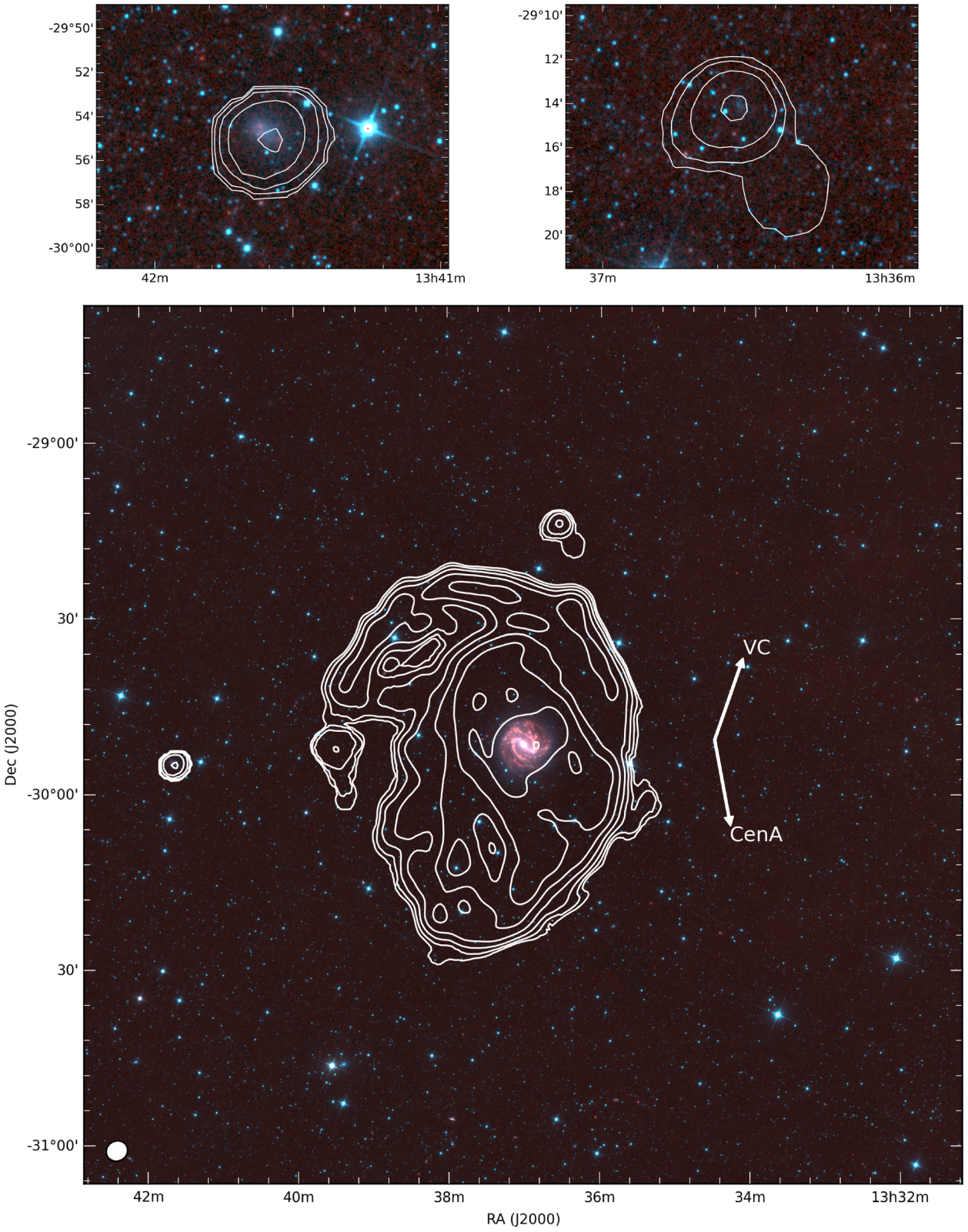

Figure 8. H I column density contours (same levels as in Fig. 6), overlaid on the three-colour *WISE* image. In this image, the blue channel is formed from *W*1 and *W*2, the green channel from *W*1, *W*2, and *W*3, and the red channel from *W*3 and *W*4. Each channel is displayed using a square root stretch. The two arrows indicate the directions towards the Virgo Cluster and the Centaurus A group. Note that UGCA 365 is visible to the north of the extended disc of M83 itself, and NGC 5264 to the east. These companions are shown in greater detail in the upper-right and upper-left panels, respectively.

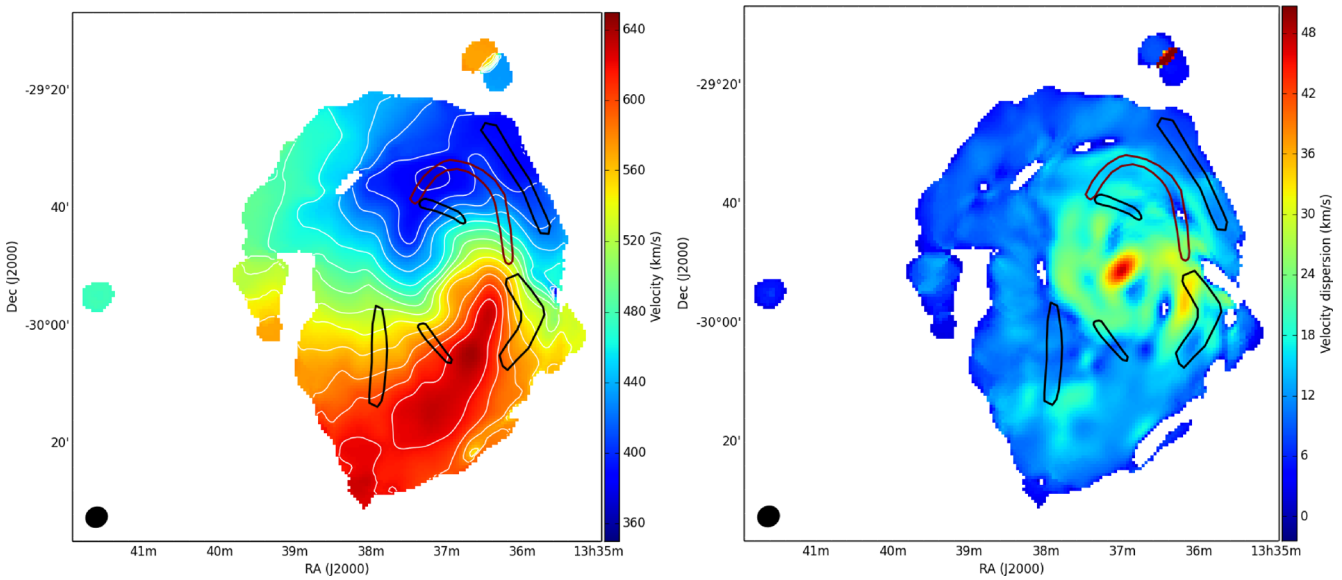

Figure 9. Velocity field (left) and velocity dispersion (right), both clipped to only display values for pixels that have column densities above 5.6e18. The beamsize is shown in the bottom left of each panel with a black ellipse.

We find an H I mass for the northern galaxy (UGCA 365) of $M_{\rm HI} = 2.7 \times 10^7\,{\rm M}_\odot$ (assuming $D = 5.26$ Mpc based on 4 TRGB measurements in NED[2]), and for the eastern galaxy (NGC 5264) we find $M_{\rm HI} = 2.5 \times 10^7\,{\rm M}_\odot$ (assuming $D = 4.66$ Mpc based on 3 TRGB measurements in NED).

The H I velocity field and velocity dispersion of M83 are displayed in Fig. 9. While the velocity field is very well behaved, it clearly shows signs of a substantial warp in the outer parts. Beyond the optical radius, the position angle twists to almost 90° from the orientation within the optical body. Twists in the isovelocity contours, particularly in the northern arm-like extension, betray the presence of substantial non-circular motions in the gas distribution. We model the structure of the H I disc in Section 3.2. The velocity dispersion map is discussed in some detail in Section 3.5, where we also consider SF in the outer disc.

In the rest of this section, we highlight some interesting aspects of the extended disc in M83, and its connection to the larger environment. Since the H I is very extended, we will address the morphology and kinematics far from the optical body. We will also discuss connections to the companion galaxies.

3.2 Tilted ring modelling

The moment maps of M83 show that the galaxy can be divided into a fairly regular and symmetric inner part, corresponding with the optical disc, and a more asymmetric and extended outer part. Of this outer part the southern (receding) half seems to be more regular (both in morphology and kinematics) than the northern (approaching) part. The angular resolution of the data does not allow a detailed in-depth study and mass-modelling of the rotation curve of M83. In this subsection, we will concentrate on the dynamics of the outer disc and the presence of non-circular motions. Uncertainties in the inner rotation curve are discussed in Section 3.3.

[2] The NASA/IPAC Extragalactic Database (NED) is operated by the Jet Propulsion Laboratory, California Institute of Technology, under contract with the National Aeronautics and Space Administration.

3.2.1 The simplest tilted-ring model

We use the intensity-weighted mean first-moment map and the tilted-rings method to explore the rotation curve of M83. We use the GIPSY task `rotcur` and adopt rings with a width of 100 arcsec (half the beam size), which Nyquist-samples the velocity field. We apply a cosine-weighting to the velocity field: each pixel is given a weight equal to the cosine of the position angle with respect to the major axis. We initially set the radial velocity component to be zero.

We first constrain the position of the dynamical centre and the value of the systemic velocity. We run `rotcur` with all parameters free (except for the zero radial velocity) and find that within $R < 1000$ arcsec the parameters are fairly stable. For these radii, the position of the centres of the rings scatters by around 30 arcsec (about one-sixth of a beam) around the optical centre. The systemic velocity here equals 510 km s^{-1} with a scatter of 4 km s^{-1}.

At radii $r > 1000$ arcsec, the behaviour is different. Here, the position of the dynamical centre changes with radius with a maximum offset of ∼130 arcsec towards larger RA and ∼360 arcsec towards smaller declination. The scatter is however as large as the offset, and for these outer rings the position of the dynamical centre cannot be determined independently. Here, the systemic velocity values decrease to ∼504 km s^{-1} with a scatter of ∼5 km s^{-1}. These changes in centre position and systemic velocity indicate that the outer rings either have a non-circular motion component or are not concentric with the inner rings (or both). We explore these possibilities later.

To get a first indication of the rotation curve, we assume that the centre positions of the rings at small radii also apply to the outer disc and we fix the position of the dynamical centre to that of the optical centre ($13^{\rm h}37^{\rm m}00.9$, $-29°51'56''$).

A second run of `rotcur` with the centre position fixed, but the remaining parameters free, shows a well-defined systemic velocity of 510 ± 2 km s^{-1} between 0 and 800″. Between 800″ and 1000″ the velocity quickly drops by 10 km s^{-1} and stays constant at a value of 500 ± 1 km s^{-1} between 1000″ and 2100″. We again assume that the values found in the inner parts apply to the entire disc.

With rotation velocity, inclination and position angle as the only remaining free parameters, we derive models for the entire velocity

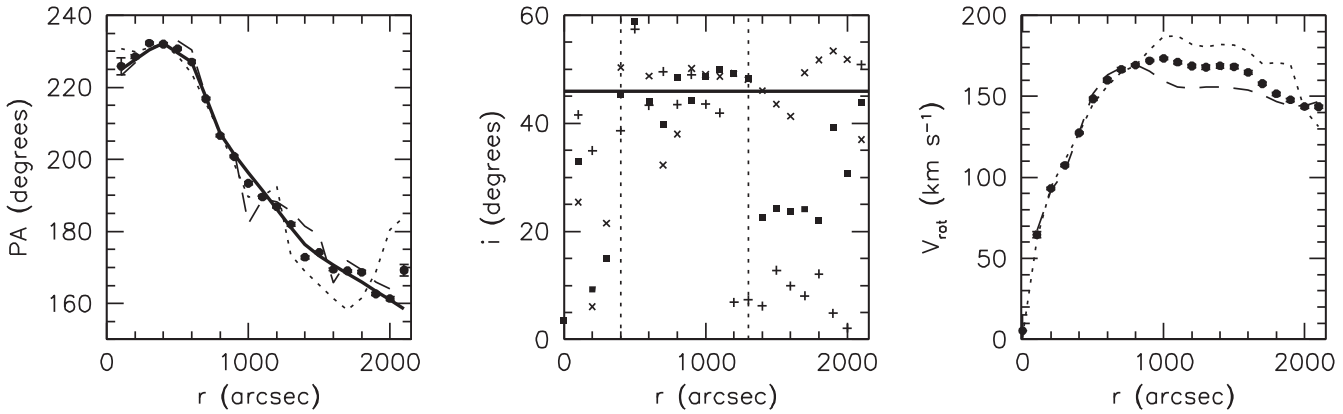

Figure 10. Model parameters for the constant systemic velocity model. Left panel shows the distribution of PA. Filled circles are the PA values found in a run with PA, inclination and rotation velocity as free parameters using the entire disc. The dotted line shows the same for the approaching side, the dashed line for the receding side. The thick solid curve show the model PA that is used for subsequent runs. Centre panel: distribution of the inclination, where only inclination and rotation velocity are free parameters and the PA is fixed to the model shown in the left panel. Filled squares show the values derived for the entire disc; ×-shaped crosses those for the approaching side; +-shaped crosses those for the receding side. The two vertical lines indicate the range over which the average value was determined, as described in the text. Right panel: rotation curve, derived with all other model parameters fixed. Filled circles show the rotation curve for the full disc, the dotted and dashed lines those for the approaching and receding sides respectively.

field, as well as the approaching and receding sides. For all three models the position angle is very well determined, and largely independent of which part of the velocity field is modelled. This is shown in Fig. 10. We describe the radial variation of the position angle using a simple multi-line-segment model, and fix this parameter in subsequent runs.

We re-run these three models, this time with only the rotation velocity and the inclination as free parameters. The model using the entire velocity field does not show a clearly preferred value for the inclination, with values ranging between 0° and almost 50°. The approaching and receding sides models show a more stable behaviour. The approaching side shows two distinct inclination ranges. At radii up to 1100 arcsec we find an average value of 44 ± 6 degrees. At larger radii a steep drop in the inclination results in values 8 ± 3 degrees. Such low values would lead to deprojected rotation velocities between ∼500 and ∼1000 km s^{-1} and it is clear these are not physical. The receding side shows the opposite behaviour. Here, the inclination yields unphysical values at radii $r < 900''$, while for larger radii the inclination is more stable with a value 48 ± 3 degrees.

Comparing the results from the approaching and receding sides, we find that the radial range between 400″ and 1300″ gives the most representative values for the galaxy overall. Interior to 400″, the fit appears to be affected by beam smearing. Between $r = 400'' - 1300''$, we find an average inclination value of 46 ± 3 (using the model based on the entire velocity field and excluding the outlying value at $r = 500''$). We adopt this value for the entire galaxy and find the rotation curve as shown in Fig. 10. The Figure also shows the rotation curves of the approaching and receding sides using the same assumptions. A position–velocity (PV) slice through a mock observation of this model (formed using the H I radial column density distribution displayed in Fig. 5) is compared with the data in Fig. 11.

For radii $r > 1000''$ we see a systematic and opposite deviation of the rotation curves of the approaching and receding sides. In the context of the purely rotational and azimuthally symmetric model, such a deviation is an indication of an incorrectly chosen systemic velocity or centre position. In the case of M83, it more likely indicates that there are asymmetries or non-circular motions in the disc that a simple tilted-ring model cannot properly take into account.

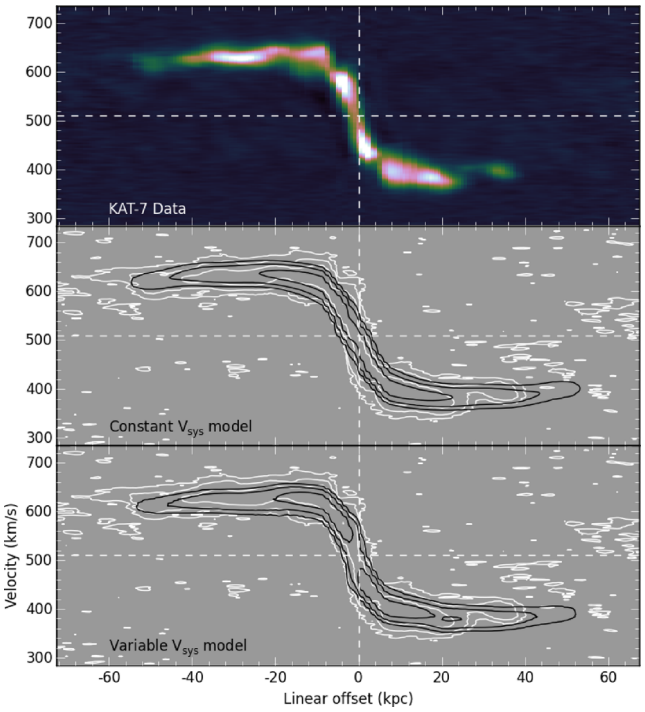

Figure 11. PV diagram constructed by following the line of nodes defined by the PA of rings in the model shown in Fig. 12. The top panel shows the data PV diagram, and the other diagrams show comparisons with the models presented in Figs 10 and 12, respectively. White contours are from the H I data cube, and black contours are from the model data cube. Contour levels start at 15 mJy beam^{-1} and increase by powers of four.

3.2.2 *Models with non-circular motions*

To explore the origins of these deviations we run a set of models where we adopt $V_{\rm sys} = 510\,{\rm km\,s^{-1}}$ for $R \leq 900''$ and $V_{\rm sys} = 500\,{\rm km\,s^{-1}}$ for $R > 900''$. As above, we again find well-constrained position angle values as a function of radius, and use a simple line-segment model to describe these. The position

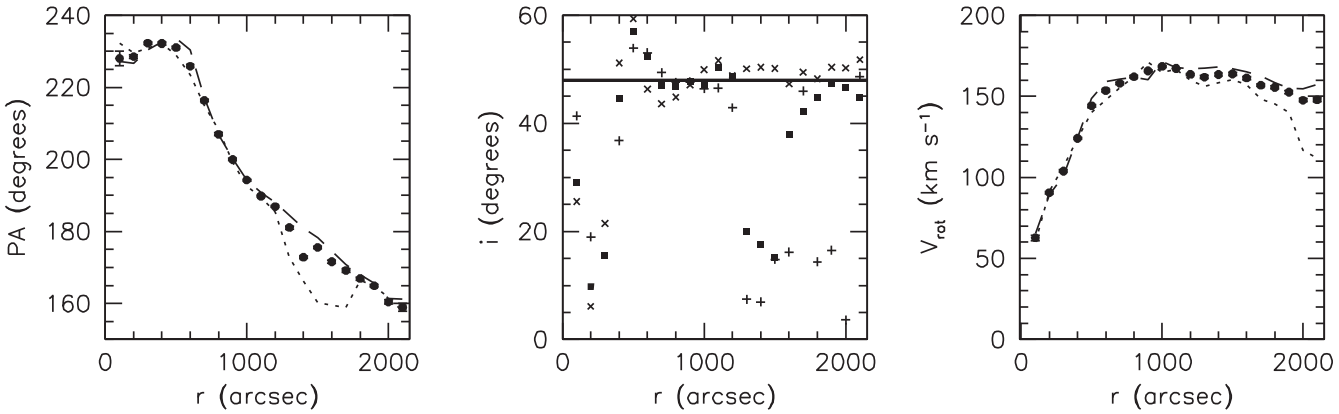

Figure 12. Model parameters assuming a variable systemic velocity of $V_{sys} = 510$ km s^{-1} inside $r = 900''$ and $V_{sys} = 500$ km s^{-1} outside $r = 900''$. All symbols and lines are as in Fig. 10, except for the centre panel, where the thick horizontal line indicates the average value of the inclination used in the modeling.

angle values are shown in Fig. 12 and are fixed to the model values hereafter.

A new run with only the inclination and the rotation velocity as free parameters again shows a large scatter in inclination. Ignoring the obvious outliers and unphysical inclination values, we use the radii between 600″ and 1200″ to determine an average value of 48 ± 1 degrees.

The receding side inclination values suggest that this value is representative for the galaxy. We therefore use this value to derive the final rotation curves. Beyond a radius of ∼1000″ the approaching and receding side rotation curves still differ substantially. Care should therefore be taken not to over-interpret the rotation curve at these large radii. A PV slice through this model is compared with the data in Fig. 11.

We investigate the uncertainty of the outer rotation curve by quantifying the effect of centre offsets and non-circular motions in the outer disc. In particular, we explore what non-circular motions or centre offsets are needed to produce a model that is consistent with a flat rotation curve with an amplitude of 165 km s^{-1} beyond $r = 1400$ arcsec. For a model where we allow the center position to vary, we find that to produce a flat rotation curve in the outer parts, the central positions of these outer rings only need to change by ∼200 arcsec, or less than one beam. Similarly, if radial motions are used to make the rotation curves flat, only about 10 km s^{-1} of radial motions are needed.

Comparing the various models derived in this section, we therefore conclude that under the various assumptions presented here the outer rotation curve is uncertain by about ±20 km s^{-1}. These unconstrained rotation velocities at large radii thus provide only limited information about the dark matter distribution in the outer disc of M83.

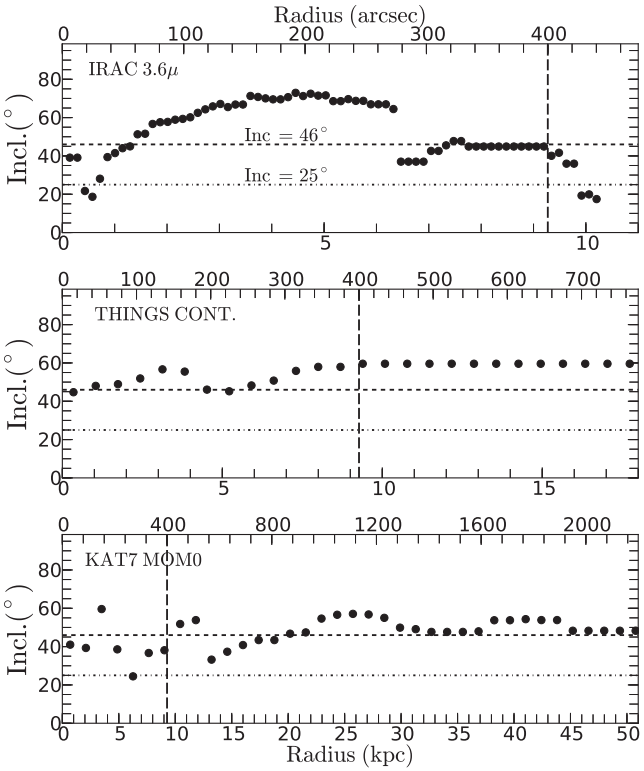

Figure 13. Comparison of the inclinations derived from isophotal fitting of the IRAC 3.6 μm image, the THINGS (natural weighting) continuum image (de Blok et al. 2008) and the H I total intensity map from our KAT-7 data. The horizontal dotted lines show inclinations of 25° and 46° and the vertical dashed lines show the radius of 400 arcsec.

3.3 Discussion of the RC and comparison with previous H I studies

The last section (see Figs 10 and 12) has shown clearly that while the variation of the PA from 230° to 160° is very well defined by the tilted ring analysis, the variation of the inclination for $r < 400$ arcsec and $r > 1200$ arcsec is much less constrained, being more or less constant ∼46° between those two radii. In order to try to constrain better the inclination, it was decided to use means other than the kinematics. Fig. 13 compares the inclinations derived from isophote fitting of the IRAC 3.6 μm image (Barnes et al. 2014), the THINGS (natural weighting) continuum image (de Blok et al. 2008) and the H I total intensity map from our KAT-7 data. For the continuum, the THINGS data were adopted because of their better spatial resolution, which is important for the inner parts.

We first looked at the IRAC 3.6 μm image. While the inclination is not well defined in the inner 50 arcsec (35°.2 ± 9°.8), it tends toward more edge-on values for 50 arcsec $< r <$ 250 arcsec

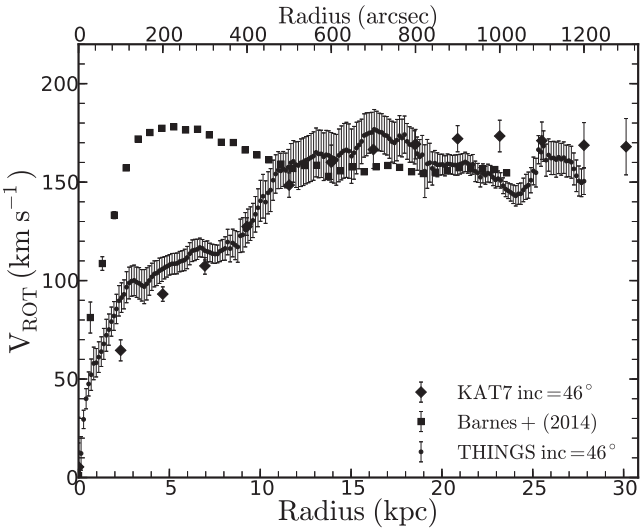

Figure 14. Comparison of the KAT-7 rotation curve with the ones from THINGS (de Blok et al. 2008; Barnes et al. 2014).

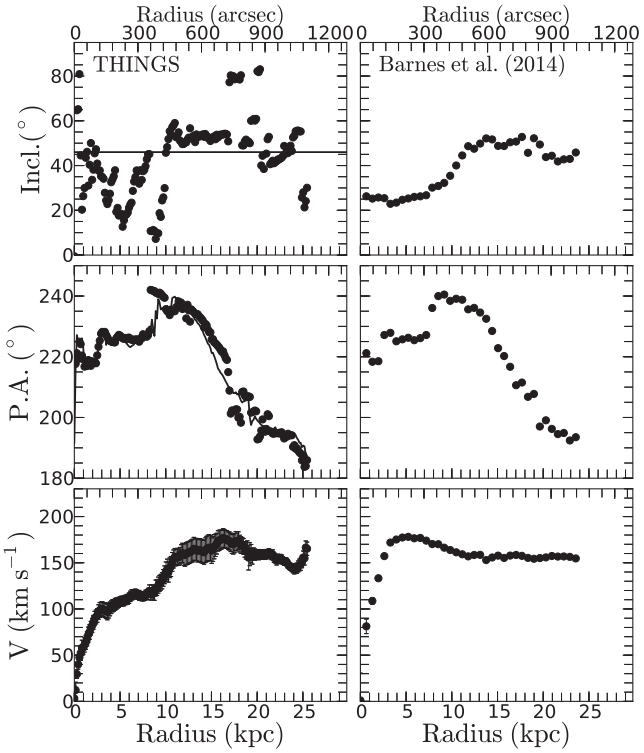

Figure 15. Comparison of the kinematical parameters determined from the H I data presented by de Blok et al. (2008) and Barnes et al. (2014). On the left, the dots are from a ROTCUR solution with i and PA left free to vary. The continuous lines illustrate the adopted parameters. On the right, we show the i and PA values that correspond to the rotation curve determined by Barnes et al. (2014).

(65.°0 ± 6.°2) and intermediate in the disc region for $r > 250$ arcsec (43.°3 ± 12.°1). However, this infrared image is probably not very useful to constrain the disc inclination since the isophotes between 50 arcsec $< r <$ 250 arcsec trace the morphology of the inner bar rather than the disc, which explains the very high implied inclination values. For the continuum image, we obtain an inclination of 51.°4 ± 5.°0 for $r <$ 400 arcsec and 55.°5 ± 5.°4 over the whole radius range. Finally, we consider a fit to the isophotes of our KAT-7 H I total intensity map. It can be seen again that the inclination is not well constrained for $r <$ 400 arcsec (39.°7 ± 10.°4) but is quite constant out to the largest radius (47.°5 ± 7.°6).

From all of these comparisons, we conclude that a constant inclination of 24° as adopted by Park et al. (2001) is not justified from our analysis. Moreover, such a face-on orientation would imply very large rotation velocities of ∼300 km s^{-1} at r ∼15 arcmin implying an absolute magnitude $M_B \sim -23$ (Persic & Salucci 1991; Persic, Salucci & Stel 1996), which is very bright when compared to the absolute magnitude ∼−21, estimated for M83 at our adopted distance (see Table 1). The actual absolute magnitude is compatible with our assumed inclination of 46° and the corresponding maximum velocity ∼170 km s^{-1}.

In order to be able to consistently compare the available data, a constant inclination of 46° was adopted for the rotation curves derived from KAT-7 (this work) and one derived for the VLA (THINGS) data (note that de Blok et al. 2008 did not derive a rotation curve for M83 in their paper). Fig. 14 compares those two rotation curves with the one derived by Barnes et al. (2014), also from VLA data. First, if we compare the KAT-7 and THINGS rotation curves, we see that they agree fairly well between 300 and 800 arcsec. Some beam smearing is apparent for $r <$ 300 arcsec, and the KAT-7 rotation velocities are 10–20 km s^{-1} higher around 1000 arcsec before becoming consistent with the outermost THINGS value around 1100 arcsec. On the other hand, while all three rotation curves are in agreement for $r >$ 400 arcsec, the velocities from Barnes et al. (2014) are much higher in the inner parts. This can be understood easily through comparison with Fig. 15. While the rotation curves from both KAT-7 and THINGS were developed using a fixed inclination of 46°, Barnes et al. (2014) allowed the inclination to go down to ∼20° in the inner parts, resulting in much higher rotational velocities.

Because of the uncertainties in the inclination for $r <$ 400 arcsec and $r >$ 1200 arcsec, no attempt will be made in this paper to derive mass models for M83 since the inner parts (strong gradient) are crucial to distinguish between cored (e.g. ISO) and cuspy (e.g. NFW) dark matter profiles and the outer parts for MOND models.

3.4 Environment and interactions

By comparing the data velocity field with the velocity field derived from our tilted ring model, we can identify deviations from pure circular rotation and the simple geometry incorporated in the modelling. In the central parts of the galaxy, the velocity deviations are small (≈0 ± 8 km s^{-1}) and consistent with the star-forming disc being well behaved. At intermediate radii, there is a spiral shape to the velocity residuals that is consistent with the outer H I arm morphology. These arms are oriented with a pitch angle opposite in sign with respect to the optical arms (i.e. counter-clockwise winding, as opposed to clockwise winding in the inner disc and far outer parts). This may be the sign of a past retrograde interaction. In the residual velocities, we also note a large-scale gradient (magnitude ±50 km s^{-1}) from east to west in the far outer parts. This may be a consequence of the apparent offset in rotational velocity from approaching to receding side (see Fig. 10), and/or may indicate that a small shift in the dynamical centre is appropriate for the outer rings (see Section 3.2).

The stellar stream that has previously been catalogued as KK 208 is visible in Fig. 6. The stream's shape and extent is outlined for clarity in the optical image, as well as in the H I column density

map, velocity field, and velocity dispersion map. The stream clearly has a recognizable signature in the kinematics of the H I disc. Systematic twists in the isovelocity contours coincide with the location of the stream, indicating that the stream has had a gravitational influence on the outer-disc gas. This provides additional evidence that the stellar stream is the remnant of the object that interacted with the outer disc of M83 (see also Barnes et al. 2014), causing its disturbed outer-disc morphology and kinematics, and potentially creating the conditions needed to initiate the prominent outer-disc SF. With future deep H I followup observations (e.g. with MeerKAT), the details of the H I in this region can be studied at similar surface brightness sensitivity but much higher angular resolution, shedding more light on the environmental effects that have helped to shape M83.

3.5 Outer-disc SF and velocity dispersion

With our H I data at its relatively coarse angular resolution, we are only able to broadly compare the distribution of outer-disc SF to the neutral gas distribution. As compared with the strong spatial correlation described by Bigiel et al. (2010), we can only confirm that the regions of SF are co-located with local enhancements in H I column density. An overlay of the neutral gas distribution on deep *GALEX* imaging is shown in Fig. 16. Note that the two stellar stream segments most closely connected to the main optical disc are seen in *GALEX* as outer-disc spiral arms, as well as in the deep optical image (Fig. 6). The loop-like stellar stream is not visible with *GALEX*. This is consistent with the loop structure having a different origin than the outer-disc star-forming arms.

On the other hand, a large mass of H I is present in the outer parts of M83 and *unassociated* with ongoing SF. For the most part, this gas distribution was not recovered with the much higher angular resolution VLA observations (see Fig. 7). Much of the discrepancy in recovered H I mass is attributable to a lack of surface brightness sensitivity in the THINGS data (Fig. 4 and Section 3.1). We therefore conclude that the bulk of the outer-disc neutral gas is diffuse and not clumpy on scales recovered by the VLA, supplemented with some H I overdensities tracing arm structures that became gravitationally unstable, allowing outer-disc SF to proceed.

We conclude this discussion with a brief look at the H I velocity dispersion (Fig. 9). Enhancements in velocity dispersion may be related to SF properties and their impact on the interstellar medium (ISM; e.g. Ianjamasimanana et al. 2015), providing additional leverage on the relationship between gas and SF. However, we find that in our low-resolution KAT-7 H I data, systematic resolution effects provide a dominant contribution to the velocity dispersion in particular regions. At the innermost radii, beam smearing causes the highest dispersion values ($\gtrsim$40 km s^{-1}; see Fig. 9). At intermediate radii, many of the regions of high-velocity dispersion tend to align with locations where tilted rings in our unconstrained models (Section 3.2) overlap due to projection effects. This is borne out by the appearance of the line profiles in those locations, which are reminiscent of the superposition of more than one velocity profile within the large beam rather than broadening of a single profile. An analysis of the H I velocity dispersion must therefore await higher angular resolution observations. Although M83 is not part of the MHONGOOSE sample (because mosaicking is required), we emphasize that our KAT-7 data provide a strong case for a MeerKAT early science programme focused on deep high-resolution mapping of the H I in this system.

3.6 Disc edge

A prominent feature of the H I disc of M83 is the sharp edge to the gas distribution, which is clearly visible as a close packing of the outermost contours in e.g. Fig. 8. This edge may be an indication of dynamical effects in the environment, ionization effects from the IGM, or some other physical effect.

Before discussing possible physical origins for this morphological feature, we first investigate whether the apparent sharp edge in the H I disc could be caused by technical issues. First, we test whether the mask applied in the creation of the column density image could artificially truncate the edge of the H I disc. We have repeated the same procedure for creating the column density map, but using a mask expanded in all three coordinates of the input data cube. Specifically, we took the binary 3D mask and smoothed it (using a 7-pixel boxcar kernel in velocity, and a Gaussian beam with FWHM = 450 arcsec – twice the size of the synthesized beam – in the angular dimensions). We then formed a new binary 3D mask by clipping the smoothed result at the 50 per cent intensity level. Visual inspection confirmed that the new mask provides much more empty space at the outer edge of the disc. Recreating the column density map, using this new mask in the summation step, led to very little difference in the outer-disc morphology. We conclude that the masking step has not artificially sharpened the disc edge.

As a second test, we have formed a total intensity image using a completely different approach that does not impose any morphological constraints. In this procedure, we identify the peak velocity in each spatial pixel, and shift the corresponding spectrum so that their peaks are all aligned at the same velocity (0 km s^{-1}). In this resulting 'shuffled' cube, we integrated the central 45 velocity pixels (67.5 km s^{-1}) without any masking. This leads to an integrated intensity map with improper values in the central parts (where typical velocity widths exceed the summation range used here), but with accurate morphology in the outer parts, including a sharp edge similar in behaviour to what is observed in our adopted column density map (and particularly on the western edge of the disc). This confirms that the sharpness of the H I disc is robust to the details of creating the column density map.

A final technical point to consider is the possibility of missing flux on large angular scales due to a lack of short spacings. As highlighted by Lucero et al. (2015), the sensitivity of KAT-7 to emission on large scales is particularly good for an interferometer. Moreover, we have demonstrated in Section 3.1 that the total H I mass that we have determined is fully recovered with respect to single-dish measurements. Yet locally, some missing flux is possible. Based on inspection of the column density map constructed using the expanded mask described above, we can identify regions of negative flux adjacent to the disc edge in some regions, and the histogram of column density values is non-Gaussian at negative values. The minimum column density value is -1.96×10^{19} cm^{-2}, or only -3.5σ with respect to the nominal column density sensitivity in Table 5. The integral of negative column densities only comes to 0.3 per cent of the integral of positive column densities. We consider it unlikely that this slight negative bowl can be responsible for the sharp edge, but cannot exclude that it has an impact on the morphology in localized regions. We discuss the possible effect as we proceed.

To quantify the structure at the edge of the disc, we have isolated five regions where the local morphology is relatively regular. Due to the large-scale and prominent asymmetries in the outer disc, we cannot simply study an azimuthally averaged radial profile. Instead, for each region we have constructed an average profile perpendicular to the disc edge (identified by tracing the $N_{\rm H\,I} = 10^{19}$ cm^{-2} contour).

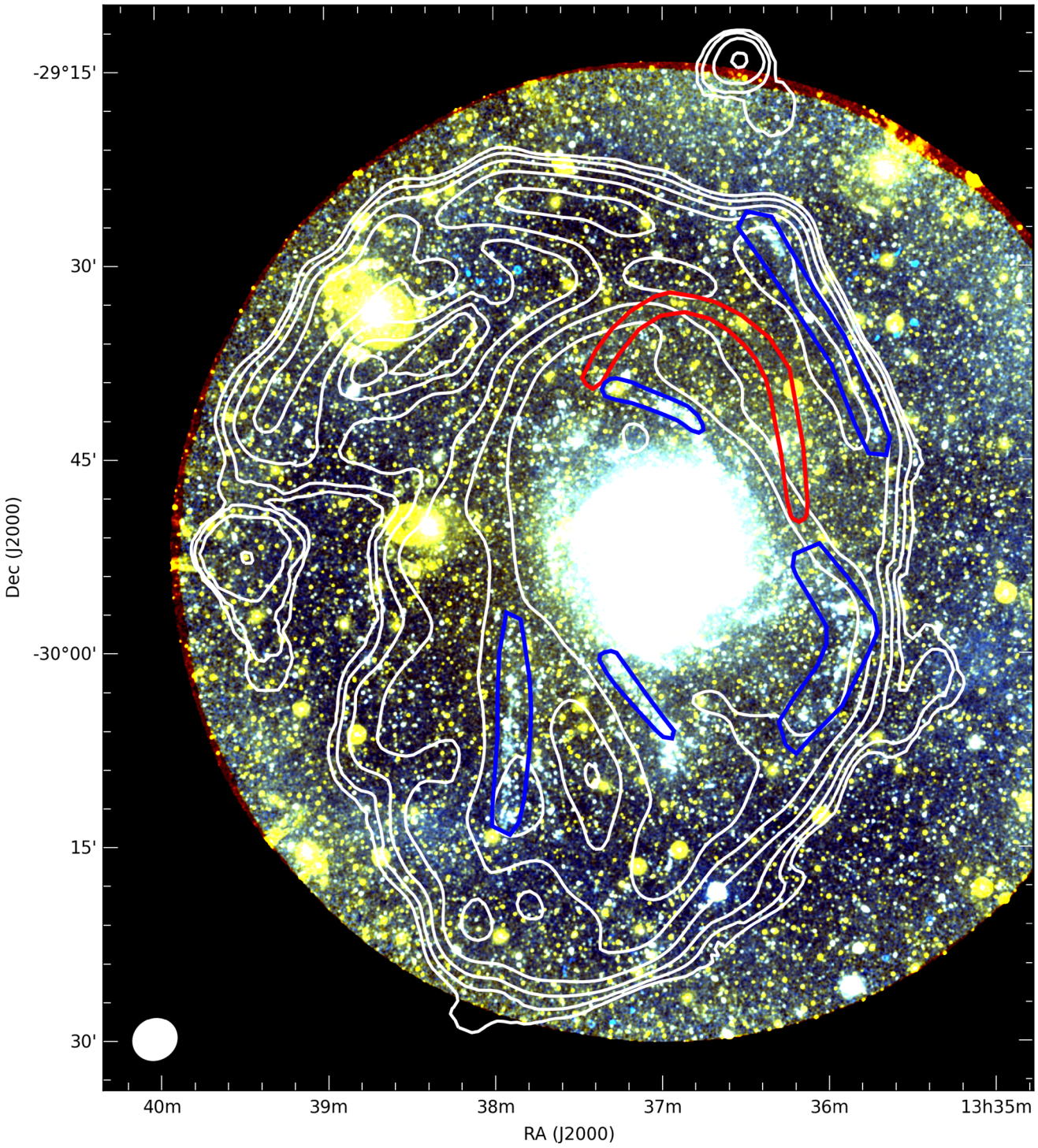

Figure 16. Overlay of KAT-7 H I column density distribution on a false-colour image formed from *GALEX* NUV and FUV images, both smoothed to 10 arcsec. The colours are chosen such that FUV emission appears blue. The H I column density contour levels are the same as in Fig. 6. The beam size is shown with a white ellipse in the bottom-left corner.

These average profiles are shown in Fig. 17. Each average profile was fitted with both an exponential and a Gaussian function (between the $N_{\rm HI} = 5.6 \times 10^{18}$ cm^{-2} and $N_{\rm HI} = 5.6 \times 10^{19}$ cm^{-2} levels) to obtain characteristic length-scales. In each case, whichever functional form led to a fit with a lower covariance was adopted. The fitted functions are shown with the data points in Fig. 17. It is remarkable that in all regions the characteristic length-scale is very short: in most regions $\lesssim$2 kpc (cf. the beamsize of our observations, $\approx$5 kpc). In fact, the column density profiles demonstrate that the average column density drops by an order of magnitude within such a characteristic length-scale.

This kind of sharp disc edge is very similar to the situation in NGC 3198 (see Maloney 1993), from deep VLA observations with similar column density sensitivity compared to our KAT-7 data. In NGC

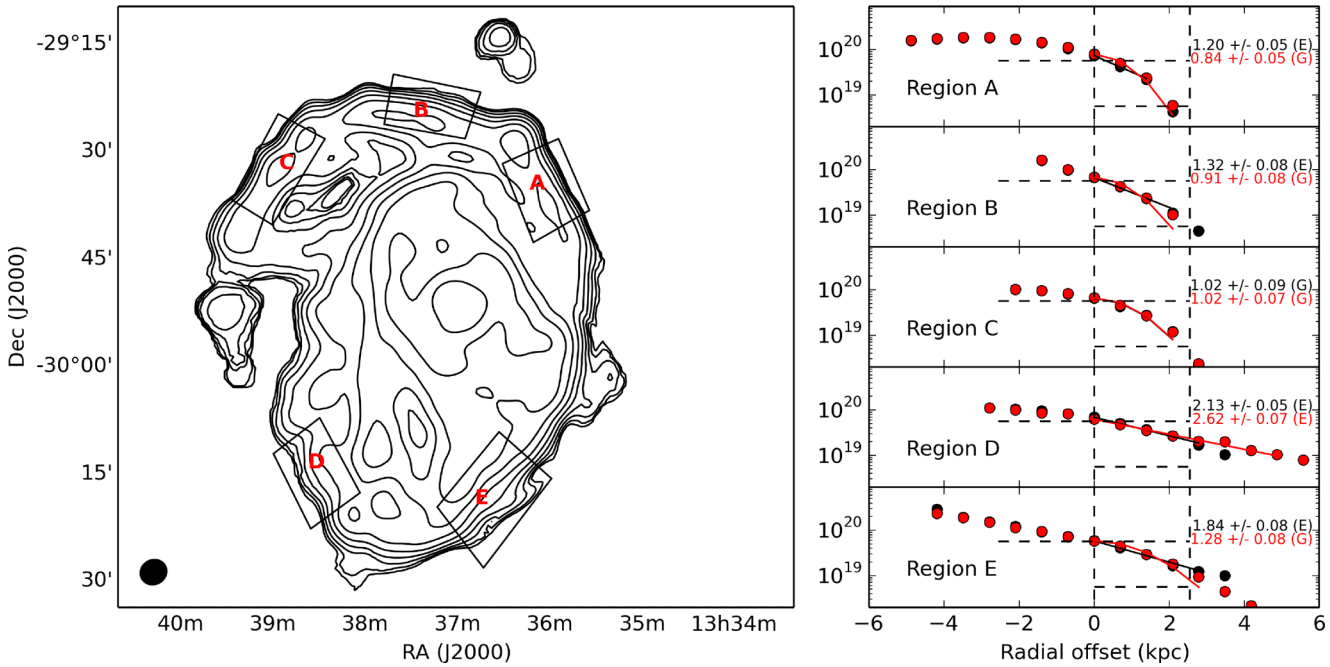

Figure 17. Sharpness of H I disc edges. The left-hand panel shows the column density map, with five regions indicated. The average run of column density perpendicular to the disc edge for each region is shown in the right-hand panels. The points are from the adopted column density map (black), and from the one created using an expanded mask (red). Lines show fits to the data points with characteristic length scales as indicated in the legend of each panel. Here, 'G' indicates a Gaussian fit and the given value is the fitted value of σ. An 'E' indicates an exponential fit and the given value is a scalelength. In both cases, the values are given in kpc. The typical length-scale corresponding to the synthesized beam size is shown by the vertical dashed lines. The zero-point of the radial offset is at the point where the average column density crosses the $N_{\rm HI} = 5.6 \times 10^{19}$ cm^{-2} level (upper horizontal dashed line), and the lower horizontal dashed line indicates the $N_{\rm HI} = 5.6 \times 10^{18}$ cm^{-2} level. In most cases, the average column density drops by an order of magnitude within about a beamwidth, or 2–3 kpc. The beamsize itself is shown with a black ellipse in the bottom-left corner of the left-hand panel.

3198, too, the azimuthally averaged H I column density distribution drops sharply (∼order of magnitude within 3 kpc) at the edge of the disc, from $N_{\rm HI} = 5 \times 10^{19}$ to 4×10^{18} cm^{-2}. This implies a disc sharpness of $\Delta R/R \lesssim 0.1$ where ΔR is the characteristic length-scale of the disc edge. In the case of M83, we have $\Delta R/R \lesssim 0.03$. Maloney (1993) models the H I edge in NGC 3198 as an ionization effect; the intergalactic radiation field photoionizes the rarified gas in the far outer parts up to a characteristic column density consistent with that at the edge of NGC 3198, and, we now see, of M83 as well. An implication of the photoionization interpretation is that the outer-disc gas distribution is smooth, not clumped into clouds. This is consistent with our picture of the outermost H I in M83 that we developed when contrasting the VLA THINGS and KAT-7 data sets.

An alternative mechanism for producing a sharp disc edge is a ram pressure interaction with the surrounding IGM, as has been proposed for NGC 300 by Westmeier, Braun & Koribalski (2011, see also references therein). If M83 is moving through the IGM at a close to face-on trajectory, the sharp disc edge that we observe could represent the truncation radius where ram pressure dominates over the stabilizing gravitational pressure. Beyond that radius, no equilibrium is possible in this picture regardless of the vertical gas distribution. However, just inside the truncation radius the transition between dominance of ram pressure and the gravitational restoring force would be a function of the vertical gas distribution and this would then be responsible for the detailed morphology of the steep decline in H I column density at the disc edge. Because we are unable to develop a reliable model of the dark matter halo in which M83 resides (see Section 3.3), we cannot constrain a quantified estimate of the impact of ram pressure in a similar fashion to Westmeier et al. (2011). However, we do note that for the conditions simulated in that paper (IGM density, and relative velocity of galaxy and IGM), the predicted transition radius occurs where the H I column density declines to $N_{\rm HI} \sim 10^{19}$ cm^{-2}, which is also the characteristic value at the H I disc edge in M83.

Finally, we point out that the sharpness of the H I disc seems slightly enhanced towards the northern side of the galaxy, as compared to the south side of the galaxy. The sharper cutoff is visible by eye when inspecting the column density contours, and is also reflected in the shorter characteristic scalelengths presented in Fig. 17 for regions A, B, and C when compared to those in regions D and E. In the ionization scenario, this may be a result of a higher extragalactic ionizing photon flux from the northern direction. Alternatively, if ram pressure is the dominant effect in the outskirts of M83, a northern component to the 3D trajectory of the galaxy might be indicated rather than a purely face-on interaction with the IGM. Sensitive observations of the extended H I distribution in nearby galaxies will be one of the outcomes of the MHONGOOSE survey, and it may become possible to draw a correspondence between disc edge sharpness and the properties of the environment, including the ionizing photon flux encountered by the sample galaxies from various directions.

4 RADIO CONTINUUM POLARIZATION AND MAGNETIC FIELDS

Our initial observation of M83 was a broad-band full-polarization continuum track, which we followed up with the line observations described in Section 3. In future, the MeerKAT correlator will be capable of creating both the broad-band data set simultaneously with

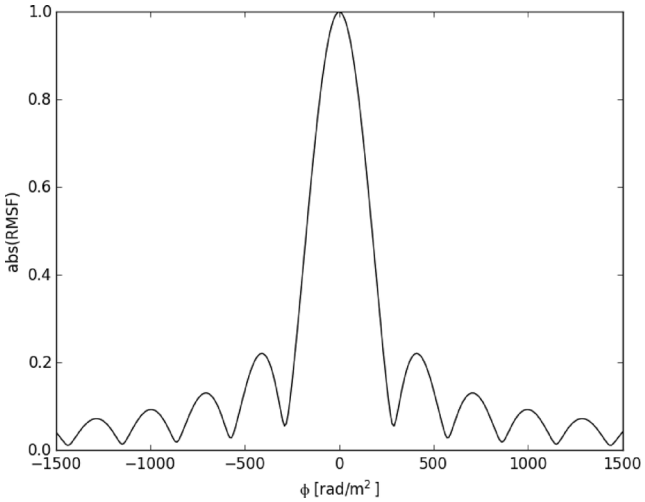

Figure 18. The RMSF resulting from the KAT-7 continuum data presented in this paper.

the high-velocity resolution line band. This will allow the study of the H I structure and kinematics, while also probing the magnetic fields within the same objects.

To characterize the ordered component of the magnetic field in M83, we have created a series of narrowband images in Stokes Q and U as described in Section 2.1, and processed them using the rotation measure (RM) synthesis (Brentjens & de Bruyn 2005) technique. This procedure performs a Fourier transform operation to translate Q, $U(\lambda^2)$ into Q, $U(\phi)$. Here, λ is the observing wavelength and ϕ is the so-called Faraday depth, which corresponds to the Faraday RM in simple situations.

The instrumental response function describing the ability to recover polarized emission at a precise Faraday depth is commonly referred to as the rotation measure spread function (RMSF). The RMSF from this wideband observation with contiguous frequency coverage is well behaved, as shown in Fig. 18. The FWHM of the main peak is 320 rad m^{-2}, and the sidelobes are fairly low in magnitude ($\lesssim$20 per cent). Due to the relatively low frequencies that we have employed, the maximum scale of RM structure that can be recovered is only 73 rad m^{-2}, less than the FWHM of the RMSF. This means that we are insensitive to Faraday thick emission (i.e. polarized emission that is present from a broad range of Faraday depths), which would originate for example from a medium extended along the line of sight that is both emitting polarized synchrotron radiation and causing Faraday rotation (see, e.g. Sokoloff et al. 1998). In effect, our wideband KAT-7 observations are only capable of recovering Faraday screens. For comparison with the polarization properties at higher radio frequencies, we refer the reader to Frick et al. (2016).

After RM synthesis, a cube is obtained that has Faraday depth as its third axis. Each frame contains the amount of polarized emission that has experienced a certain amount of Faraday rotation. This cube can be interpreted similarly to an H I cube. In particular, we extract the peak value along each spectrum to obtain the linear polarization map, and record the corresponding Faraday depth at the location of the peak polarization to generate an RM map. This 'moment' analysis was justified by inspecting the Faraday spectra to ensure that there were no complicated features (emission present over a broad range of Faraday depth). This simple approach therefore provides a reasonable reproduction of the polarized emission at these frequencies. The corresponding results are shown in Fig. 19.

The polarized emission recovered in this way from our KAT-7 data is found to be distributed in an asymmetric fashion across the optical disc, in the sense that the approaching side (see Fig. 9) is relatively highly polarized, but the receding side shows very little polarization. This large-scale pattern is in excellent agreement with many other spiral galaxies observed in polarization at similar frequency (see Heald, Braun & Edmonds 2009; Braun et al. 2010; Vollmer et al. 2013) and is consistent with early polarization mapping of M83 at similar radio frequency (Sukumar & Allen 1989, see also Neininger et al. 1993). The orientation of the magnetic field vectors from the KAT-7 data is largely as expected, despite the low angular resolution, in that it follows the optical spiral pattern to a large degree. By comparison to the magnetic field distribution presented by Frick et al. (2016), we can see that the northern region of M83 is dominated by magnetic fields tracing the spiral pattern, while the eastern side is dominated in polarization by magnetic fields following the bar orientation. At the easternmost edge, our derived magnetic field orientation appears at first glance to be contradictory to the polarization vectors presented by Sukumar & Allen (1989), but on further inspection the apparent difference seems to be resolved when taking into account the RM values in that region. To the south, the little polarization that is present at these low frequencies again follows the spiral pattern.

Note that the resulting average magnetic field orientation ($209\overset{\circ}{.}8 \pm 3\overset{\circ}{.}7$) is approximately parallel to the major axis (PA $\approx 225^\circ$; see Fig. 10). This seems to be consistent with the prediction by Stil et al. (2009), who demonstrate that an unresolved and idealized galaxy should show an average polarization angle (perpendicular to the mean magnetic field direction) oriented along the minor axis. The agreement between prediction and reality in this case is somewhat surprising given the substantial asymmetries in the polarized intensity from M83 that are caused by the strong bar pattern, and strong localized depolarization that is systematically associated with the receding major axis as seems to be the case throughout the spiral galaxy population (e.g. Braun et al. 2010). Whether this consistency with predictions is broadly true at these frequencies in a larger sample of galaxies remains to be seen, but will be important for interpretation of weak gravitational lensing signals that depends on polarization for a reference orientation (Brown & Battye 2011). Polarization observations at higher frequencies are important for unresolved galaxies, to avoid systematic effects such as depolarization biasing the recovery of the average polarization angle.

The RM map corresponding to the polarized intensity is also presented in Fig. 19. We note that the foreground Milky Way RM value is -28.5 ± 10.7 rad m^{-2} (Oppermann et al. 2015). The bright approaching side shows Faraday rotation at a value similar to the foreground value, but the faint receding side displays an overall positive Faraday depth contribution. While our new RM map is broadly consistent with the higher frequency RM maps from previous efforts, particularly given its lower angular resolution, there are differences that are possibly related to our lower observing frequency that probes the magnetic field at larger vertical distance from the mid-plane where depolarization effects are weaker. Taken together with the higher frequency RM from Neininger et al. (1993) and Frick et al. (2016), the change in sign of RM across the minor axis could suggest a large-scale field with a change in magnetic field directionality above the disc. Since the RM errors are dominated by low signal to noise (particularly in the receding side of the galaxy), deeper observations will be required to lower the uncertainties and confirm that the Faraday RM indicate a large-scale ordered field in the disc–halo region.

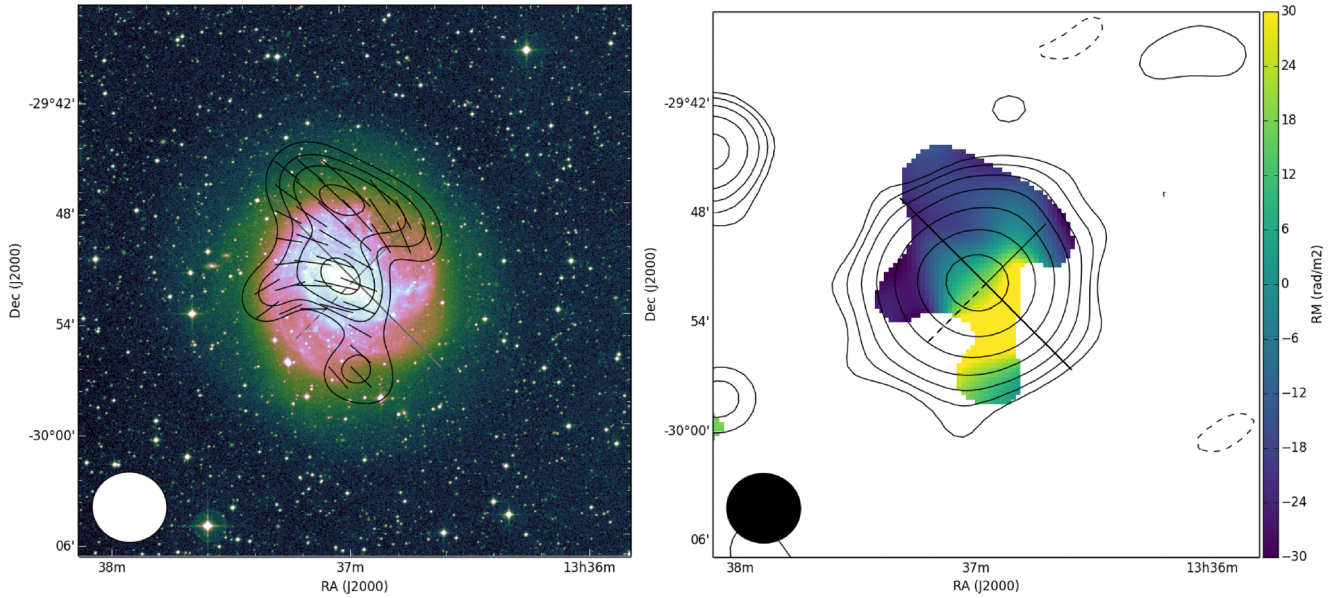

Figure 19. Polarization map and magnetic field vectors (left) and associated Faraday RM (right). In the left-hand panel, the contours are at 8,10,12,15 mJy beam^{-1} and the background is the POSS2/UKSTU Red image. The dark grey lines indicate the major (solid) and minor (dashed) axes; the kinematically receding side is to the southwest. The magnetic field vectors have been corrected for Faraday rotation, using the values in the right-hand panel. In the right-hand panel, the contours correspond to the total intensity continuum radiation, and are the same as in Fig. 1.

We conclude by noting that future polarization observations of distant galaxies will have similar physical resolution as our current KAT-7 observation of M83. The angular resolution here is 244 arcsec × 230 arcsec. Thus, we can expect that anticipated observations with greatly improved resolution (≈5 arcsec) will recover the magnetic field structure on the same physical scales, but at redshift $z \approx 0.06$. Through the detailed study of nearby objects like M83 and comparison with sensitive but low angular resolution data from KAT-7, we are better able to understand future observations of distant targets.

5 CONCLUSIONS

We have presented new observations of the nearby grand-design spiral galaxy M83, performed with the KAT-7 radio interferometer in South Africa. Located on the site of the forthcoming MeerKAT radio telescope, and later SKA1-MID, KAT-7 is not only serving as an engineering testbed for the SKA-Mid precursor, but is also helping to develop the science case for MeerKAT survey projects such as MHONGOOSE.

With our new observations, we have found that the H I distribution of M83 is more extended and diffuse than previously recognized. While outer-disc SF is closely coupled with clumpy, small-scale H I features, a more extended and diffuse neutral gas component is also present. The morphology and kinematics of the extended H I are consistent with a tidal interaction in the past, and we suggest that the northern stellar stream (previously catalogued as KK 208) may be the remnant of the interloper responsible for the disturbance. We also study the sharp edge of the H I distribution and conclude that its abrupt termination (column density declining by an order of magnitude within a couple of kpc) is not an artefact but reflects a real change in the state of the ISM material in the far outer parts. Whether variations in the sharpness at various locations around the disc reflect directional variations in the ambient intergalactic ionizing radiation field or instead reflect the direction of motion of M83 through the IGM remains to be tested with future observations.

The magnetic field distribution in M83 was also probed with our KAT-7 observations. We find that the morphology of the polarized radiation can be understood in the context of both higher resolution and higher frequency polarization observations, and in comparison with the polarization properties of the broader spiral galaxy population. It may not always be the case that unresolved (or nearly unresolved) galaxies have a close relationship between optical position angle and the position angle of the linear polarization vector; asymmetries within the galaxy such as bars and systematically depolarized regions may serve to change the averaged polarization angle.

These observations help to set the stage for the MHONGOOSE survey, which will perform similarly sensitive H I observations at much higher angular resolution for tens of nearby galaxies, while simultaneously collecting more sensitive and resolved polarization data.

ACKNOWLEDGEMENTS

We thank the KAT-7 team for supporting these observations and for their invaluable help in understanding the instrument and its calibration. We also thank David Malin for permission to use his deep image of M83, created from data that were derived from plates taken with the UK Schmidt Telescope. GH would like to thank Bärbel Koribalski for a very useful discussion about an advanced draft of this paper. WJGdB was supported by the European Commission (grant FP7-PEOPLE-2012-CIG #333939). The work of CC and TJ is based upon research supported by the South African Research Chairs Initiative (SARChI) of the Department of Science and Technology (DST), the Square Kilometre Array South Africa (SKA SA) and the National Research Foundation (NRF). The research of DL, EE and THR has been supported by SARChI & SKA SA fellowships. LvZ acknowledges support from ASTRON's

Helena Kluyver Visitor Programme. The Digitized Sky Surveys were produced at the Space Telescope Science Institute under US Government grant NAG W-2166. The images of these surveys are based on photographic data obtained using the Oschin Schmidt Telescope on Palomar Mountain and the UK Schmidt Telescope. We have made use of the 'cubehelix' colour scheme (Green 2011) to produce several of the figures in this paper. The plates were processed into the present compressed digital form with the permission of these institutions. This research has made use of the NED, which is operated by the Jet Propulsion Laboratory, California Institute of Technology, under contract with the National Aeronautics and Space Administration.

REFERENCES

Barnes K. L., van Zee L., Dale D. A., Staudaher S., Bullock J. S., Calzetti D., Chandar R., Dalcanton J. J., 2014, ApJ, 789, 126
Beck R., 2007, A&A, 470, 539
Beck R., 2016, A&AR, 24, 4
Benjamin R. A., 2000, Rev. Mex. Astron. Astrofis., 9, 256
Bernet M. L., Miniati F., Lilly S. J., 2013, ApJ, 772, L28
Bigiel F., Leroy A., Seibert M., Walter F., Blitz L., Thilker D., Madore B., 2010, ApJ, 720, L31
Blanton M. R., Moustakas J., 2009, ARA&A, 47, 159
Booth R. S., Jonas J. L., 2012, Afr. Skies, 16, 101
Boselli A., Gavazzi G., 2006, PASP, 118, 517
Braun R., Heald G., Beck R., 2010, A&A, 514, A42
Brentjens M. A., de Bruyn A. G., 2005, A&A, 441, 1217
Briggs D. S., 1995, PhD thesis, The New Mexico Institute of Mining and Technology
Brown M. L., Battye R. A., 2011, MNRAS, 410, 2057
Carignan C., 2016, in Qain L., Li D., eds, ASP Conf. Ser. Vol. 502, Frontiers in Radio Astronomy and FAST Early Sciences Symposium 2015. Astron. Soc. Pac., San Francisco, p. 55
Carignan C., Frank B. S., Hess K. M., Lucero D. M., Randriamampandry T. H., Goedhart S., Passmoor S. S., 2013, AJ, 146, 48
Carignan C., Libert Y., Lucero D. M., Randriamampandry T. H., Jarrett T. H., Oosterloo T. A., Tollerud E. J., 2016, A&A, 587, L3
Cluver M. E. et al., 2014, ApJ, 782, 90
Condon J. J., Cotton W. D., Greisen E. W., Yin Q. F., Perley R. A., Taylor G. B., Broderick J. J., 1998, AJ, 115, 1693
de Blok W. J. G., Walter F., Brinks E., Trachternach C., Oh S.-H., Kennicutt R. C., Jr, 2008, AJ, 136, 2648
de Vaucouleurs G., de Vaucouleurs A., Corwin H. G., Jr, Buta R. J., Paturel G., Fouqué P., 1991, Third Reference Catalogue of Bright Galaxies. Volume I: Explanations and references. Volume II: Data for galaxies between 0^h and 12^h. Volume III: Data for galaxies between 12^h and 24^h. Springer, New York, NY
Elstner D., Beck R., Gressel O., 2014, A&A, 568, A104
Foley A. R. et al., 2016, MNRAS, 460, 1664
Frick P., Stepanov R., Beck R., Sokoloff D., Shukurov A., Ehle M., Lundgren A., 2016, A&A, 585, A21
Green D., 2011, Bull. Astr. Soc. India, 39, 289
Heald G., Braun R., Edmonds R., 2009, A&A, 503, 409
Heald G. et al., 2011, A&A, 526, A118
Henriksen R. N., Irwin J. A., 2016, MNRAS, 458, 4210
Hess K. M., Jarrett T. H., Carignan C., Passmoor S. S., Goedhart S., 2015, MNRAS, 452, 1617
Huchtmeier W. K., Bohnenstengel H.-D., 1981, A&A, 100, 72
Ianjamasimanana R., de Blok W. J. G., Walter F., Heald G. H., Caldú-Primo A., Jarrett T. H., 2015, AJ, 150, 47
Jarrett T. H. et al., 2012, AJ, 144, 68
Jarrett T. H. et al., 2013, AJ, 145, 6
Johnston S. et al., 2008, Exp. Astron., 22, 151
Jonas J. L., 2009, Proc. IEEE, 97, 1522
Karachentsev I. D. et al., 2007, AJ, 133, 504
Karachentseva V. E., Karachentsev I. D., 1998, A&AS, 127, 409
Koribalski B. S. et al., 2004, AJ, 128, 16
Lucero D. M., Carignan C., Elson E. C., Randriamampandry T. H., Jarrett T. H., Oosterloo T. A., Heald G. H., 2015, MNRAS, 450, 3935
McMullin J. P., Waters B., Schiebel D., Young W., Golap K., 2007, in Shaw R. A., Hill F., Bell D. J., eds, ASP Conf. Ser. Vol. 376, Astronomical Data Analysis Software and Systems XVI. Astron. Soc. Pac., San Francisco, p. 127
Makarov D., Prugniel P., Terekhova N., Courtois H., Vauglin I., 2014, A&A, 570, A13
Malin D., Hadley B., 1997, Publ. Astron. Soc. Aust., 14, 52
Maloney P., 1993, ApJ, 414, 41
Nan R. et al., 2011, Int. J. Mod. Phys. D, 20, 989
Neininger N., Beck R., Sukumar S., Allen R. J., 1993, A&A, 274, 687
Oppermann N. et al., 2015, A&A, 575, A118
Park O.-K., Kalnajs A., Freeman K. C., Koribalski B., Staveley-Smith L., Malin D. F., 2001, in Funes J. G., Corsini E. M., eds, ASP Conf. Ser. Vol. 230, Galaxy Disks and Disk Galaxies. Astron. Soc. Pac., San Francisco, p. 109
Perley R. A., Butler B. J., 2013, ApJS, 206, 16
Persic M., Salucci P., 1991, ApJ, 368, 60
Persic M., Salucci P., Stel F., 1996, MNRAS, 281, 27
Piffaretti R., Arnaud M., Pratt G. W., Pointecouteau E., Melin J.-B., 2011, A&A, 534, A109
Putman M. E., Peek J. E. G., Joung M. R., 2012, ARA&A, 50, 491
Sancisi R., Fraternali F., Oosterloo T., van der Hulst T., 2008, A&AR, 15, 189
Sault R. J., Teuben P. J., Wright M. C. H., 1995, in Shaw R. A., Payne H. E., Hayes J. J. E., eds, ASP Conf. Ser. Vol. 77, Astronomical Data Analysis Software and Systems IV. Astron. Soc. Pac., San Francisco, p. 433
Sokoloff D. D., Bykov A. A., Shukurov A., Berkhuijsen E. M., Beck R., Poezd A. D., 1998, MNRAS, 299, 189
Steer D. G., Dewdney P. E., Ito M. R., 1984, A&A, 137, 159
Stil J. M., Krause M., Beck R., Taylor A. R., 2009, ApJ, 693, 1392
Sukumar S., Allen R. J., 1989, Nature, 340, 537
Thilker D. A. et al., 2005, ApJ, 619, L79
Thilker D. A. et al., 2007, ApJS, 173, 538
Tingay S. J., Jauncey D. L., King E. A., Tzioumis A. K., Lovell J. E. J., Edwards P. G., 2003, PASJ, 55, 351
Tully R. B., 1988, Nearby Galaxies Catalog. Cambridge Univ. Press, Cambridge
Tully R. B., 2015, AJ, 149, 54
Verheijen M. A. W., Oosterloo T. A., van Cappellen W. A., Bakker L., Ivashina M. V., van der Hulst J. M., 2008, in Minchin R., Momjian E., eds, AIP Conf. Proc. Vol. 1035, The Evolution of Galaxies Through the Neutral Hydrogen Window. Am. Inst. Phys., New York, p. 265
Vollmer B., Soida M., Beck R., Chung A., Urbanik M., Chyży K. T., Otmianowska-Mazur K., Kenney J. D. P., 2013, A&A, 553, A116
Walter F., Brinks E., de Blok W. J. G., Bigiel F., Kennicutt R. C., Jr, Thornley M. D., Leroy A., 2008, AJ, 136, 2563
Westmeier T., Braun R., Koribalski B. S., 2011, MNRAS, 410, 2217

This paper has been typeset from a TEX/LATEX file prepared by the author.